FINITE STRAIN MODELING OF COUPLED THERMO-MECHANICAL BEHAVIOR OF POLYCRYSTALLINE NI-TI SHAPE MEMORY ALLOYS

A THESIS SUBMITTED TO
THE GRADUATE SCHOOL OF NATURAL AND APPLIED SCIENCES
OF
MIDDLE EAST TECHNICAL UNIVERSITY

BY

VAHID REZAZADEH

IN PARTIAL FULFILLMENT OF THE REQUIREMENTS
FOR
THE DEGREE OF MASTER OF SCIENCE
IN
MECHANICAL ENGINEERING

AUGUST 2017

Approval of the thesis:

FINITE STRAIN MODELING OF COUPLED THERMO-MECHANICAL BEHAVIOR OF POLYCRYSTALLINE NI-TI SHAPE MEMORY ALLOYS

submitted by **VAHID REZAZADEH** in partial fulfillment of the requirements for the degree of **Master of Science in Mechanical Engineering Department, Middle East Technical University** by,

Gülbin Dural Ünver
Dean, Graduate School of **Natural and Applied Sciences** _____

Prof. Dr. Raif Tuna Balkan
Head of Department, **Mechanical Engineering** _____

Assist. Prof. Dr. Hüsnü Dal
Supervisor, **Mechanical Engineering Department, METU** _____

Assoc. Prof. Dr. Özgür Aslan
Co-supervisor, **Mechanical Engineering Dept., Atılım Uni.** _____

Examining Committee Members:

Prof. Dr. Suha Oral
Mechanical Engineering Department, METU _____

Assist. Prof. Dr. Hüsnü Dal
Mechanical Engineering Department, METU _____

Assoc. Prof. Dr. Özgur Aslan
Mechanical Engineering Department, Atılım Uni. _____

Assoc. Prof. Dr. Demirkan Çöker
Aerospace Engineering Department, METU _____

Assoc. Prof. Dr. Ercan Gürses
Aerospace Engineering Department, METU _____

Date: _____

I hereby declare that all information in this document has been obtained and presented in accordance with academic rules and ethical conduct. I also declare that, as required by these rules and conduct, I have fully cited and referenced all material and results that are not original to this work.

Name, Last Name: VAHID REZAZADEH

Signature :

ABSTRACT

FINITE STRAIN MODELING OF COUPLED THERMO-MECHANICAL BEHAVIOR OF POLYCRYSTALLINE NI-TI SHAPE MEMORY ALLOYS

Rezazadeh, Vahid
M.S., Department of Mechanical Engineering
Supervisor : Assist. Prof. Dr. Hüsnü Dal
Co-Supervisor : Assoc. Prof. Dr. Özgür Aslan

August 2017, 72 pages

Shape memory alloys (SMAs) hold a significant importance in different areas such as aeronautics, adaptive structures, oil/gas down-hole, and high-temperature applications of automobile industry. Nowadays, researchers have already become well-aware of these applications and attempted to discover all the primary features of this specific smart material. Meanwhile, there is a growing effort to produce mathematical models in order to imitate the related behaviors in a precise manner. Due to the crucial need to have a fine computational model, we established a constitutive theory based on the finite strain framework of continuum mechanics. The presented thermo-mechanically coupled model can perfectly reproduce all behaviors of Ni-Ti SMAs including martensitic phase transformation, pseudoelasticity, and one-way shape memory effect. Our constitutive model is also able to investigate the strain-rate and temperature dependency of the loading conditions. This work aims at utilizing finite strain plasticity setting with purely thermodynamically consistent constitutive equations. In this framework, a user material subroutine (UMAT) is written and implemented into ABAQUS/Implicit (2016) finite element program. Verification of the model is carried out by the calibrated experimental findings which exist in the literature. Numerical simulations of developed constitutive model successfully denote the ability of our phenomenological model in capturing different memory effects of

Ni-Ti SMAs under stress-strain-temperature cycling.

Keywords: Shape memory alloys, Finite strain plasticity, Constitutive modeling, Martensitic phase transformation, Pseudoelasticity, Finite element method

ÖZ

ŞEKİL HAFIZALI ALAŞIMLARIN TERMOMEKANİK DAVRANIŞLARININ MODELLENMESİ VE SİMÜLASYONU

Rezazadeh, Vahid
Yüksek Lisans, Makina Mühendisliği Bölümü
Tez Yöneticisi : Yrd. Doç. Dr. Hüsnü Dal
Ortak Tez Yöneticisi : Doç. Dr. Özgür Aslan

Ağustos 2017 , 72 sayfa

Şekil Hafızalı Alaşımlar (ŞHA) havacılık, uyarlanabilen yapılar, petrol ve gaz kuyuları, otomotiv ve havacılık alanındaki yüksek sıcaklık uygulamaları gibi farklı alanlarda önemli bir yere sahiptir. Günümüzde, araştırmacılar bu uygulamalar hakkında farkındalığa sahiptir ve bu özel materyalin tüm temel özelliklerini keşfetmeye çalışmaktadır. İlgili davranışları kesin bir şekilde benzetimi için matematiksel modeller üretilmesi konusunda ise artan bir çaba vardır. Modelleme ve hesaplama metotları üzerinde artan ihtiyaca cevap vermesi adına, sonlu gerinme çerçevesinde bünye denklemlerini içinde barındıran bir yapısal model oluşturduk. Bu üç boyutlu termo-mekanik olarak birleştirilmiş model, martensitli faz dönüşümü, psödoelastisite ve tek yönlü şekil hafıza efekti gibi ŞHA'ların tüm davranışlarını yüksek başarım ile benzetimini hedeflemiştir. Yapısal modelimiz, yükleme koşullarının gerinim hızının ve sıcaklığın bünye davranışına olan etkisini de ele almaktadır. Bu çalışma, termodinamik olarak tutarlı yapısal denklemleri, sonlu şekil değiştirme esnekliği ile birlikte kullanmayı amaçlamaktadır. Bu çerçevede bir kullanıcı malzeme altrutini (UMAT) ABAQUS /Implicit (2016) sonlu elemanlar programına yazılıp uygulanmıştır. Modelin doğrulanması literatürde bulunan kalibre edilmiş deneysel bulgularla gerçekleştirilmiştir. Gelişmiş yapısal modelin sayısal simülasyonları, fenomenolojik modelimizin stres gerilim-sıcaklık döngüsü altında ŞHA'ların farklı hafıza etkilerini yakalama yeteneğini başarıyla

göstermiştir.

Anahtar Kelimeler: Şekil Hafızalı Alaşımlar, sonlu şekil değiştirme esnekliği, yapısal modelleme, martensitli faz dönüşümü, psödoelastisite, sonlu elemanlar yöntemi

To My Mother,
A strong and gentle soul who taught me to trust in my dreams!!!.

ACKNOWLEDGMENTS

I would first and foremost like to express my sincere gratitude and thanks to Dr. Ozgur Aslan for his unconditional support and guidance during the course of this research. My appreciation for his encouragement, patience and friendship goes beyond the limit of words. His vast knowledge on theoretical and computational mechanics has always inspired me and his perfectionism in research stimulated my motivation and creativity to put forth my best effort. I am also grateful for the freedom that he gave me in pursuing my ideas which certainly provided me the great opportunity to work as an independent researcher.

I would like to devote my sincere thanks to Dr. Husnu Dal for his enlightening and constructive advice in addition to his acceptance to become the supervisor of this thesis.

I would like to gratefully acknowledge the financial support of TÜBİTAK organization within the framework of project under grand number of "116M260-TÜBİTAK 1001".

I would also like to acknowledge the support of Glenn Research Center at The National Aeronautics and Space Administration (NASA), for their support in proceeding the idea of this research and providing vast scope of experimental data.

I am thankful to the members of CSE Lab, especially my coffee mates Reza Salatin, Senem Aktas, and Caner Camalan who have made my working environment pleasant and productive. A special and sincere thank goes to Farid Saeidi for his intimate friendship and supportive companionship during this research. I am grateful for his encouragement, patience, and outstanding assistance.

It is impossible to adequately express my gratitude to my family especially to my parents Fatemeh and Ali Rezazadeh and my supportive brother Mehdi Rezazadeh, for their endless love and support providing me the necessary faith and strength to pursue my goals.

TABLE OF CONTENTS

LIST OF TABLES

TABLES

LIST OF FIGURES

FIGURES

LIST OF ABBREVIATIONS

SMA	Shape memory alloy
SME	Shape memory effect
OWSME	One-way shape memory effect
TWSME	Two-way shape memory effect
HTSMA	High-temperature shape memory alloys
Ni-Ti	Nickel-titanium shape memory alloy
ATC	Asymmetry in tension and compression
MT	Maretensitic transformation
ECAE	Equal-channel angular extrusion
ZM	Zaki and Moumni model
FE	Finite element
FEA	Finite element analysis
FEM	Finite element method
GL	Ginzburg-Landau theory
MD	Molecular dynamics
EAM	Embedded-atom-method
LJ	Lennard-Jones
2-D	Two-dimensional
3-D	Three-dimensional

CHAPTER 1

INTRODUCTION AND OVERVIEW

1.1 Shape Memory Alloys

Among thousands of distinct materials, *Shape Memory Alloys* (SMAs) can be counted as one of the peculiar materials which are able to draw the attention of humankind to themselves. Thanks to their crystallographic structure, SMAs can remember and retaliate to their initial configuration, after a mechanical deformation. By an increase and decrease in temperature, even under high applied loads, SMAs demonstrate a considerable shape recovery. Figure 1.1 presents a schematic illustration of SMAs under loading and subsequent heating.

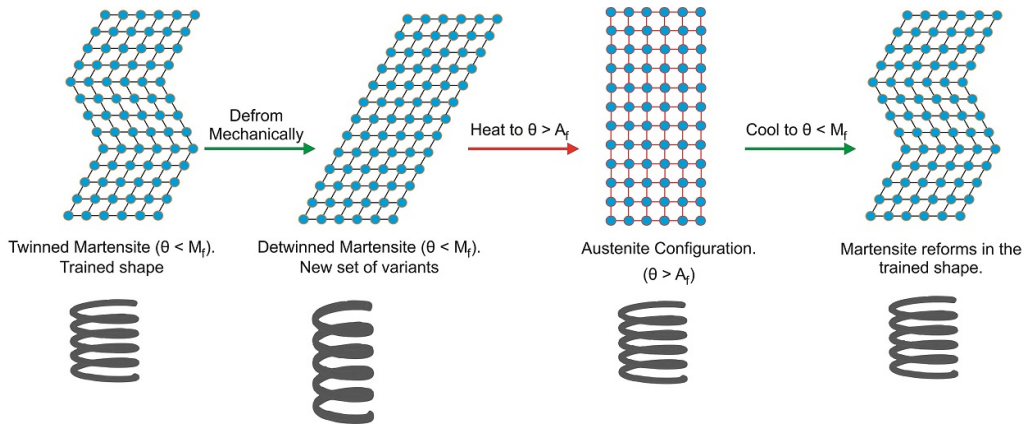

Figure 1.1: Schematic view of shape memory alloys, subjected to mechanical loading and subsequent heating. θ is temperature, M_f martensite finish temperature, and A_f is the austenite finish temperature.

Beyond unique responsive characteristics of SMAs, "Pseudoelasticity", "One-Way Shape Memory Effect (OWSME)", and "Two-Way Shape Memory Effect

(TWSME)" are considered as the main and common features of SMAs [1, 2, 3]. Following a severe deformation, OWSME enables the material to retrieve to its low-temperature state; however, in TWSME, material not only carries the memory of its low-temperature state, it can also remember its high-temperature shape. Figure 1.2, illustrates a sample, subjected to mechanical loading. Increasing temperature results in complete recovery of the sample in OWSMA while TWSME carries two different configurations, one for heated state (c), and one for the cold state (d).

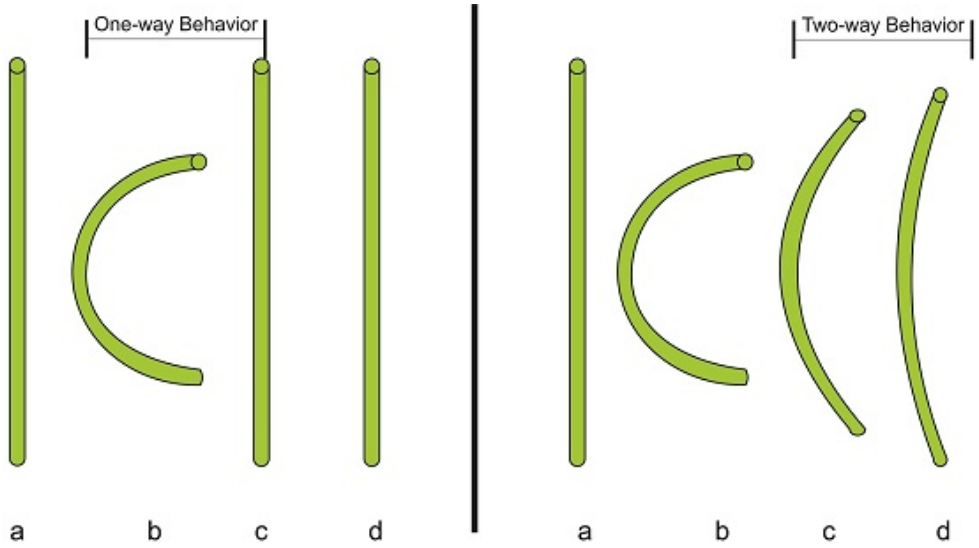

Figure 1.2: One-way shape memory effect versus two-way shape memory effect.

These alloys can absorb or dissipate mechanical energy when they are subjected to different thermo-mechanical loading. These distinctive characteristics, along with bio-compatibility have made SMAs popular in high-technology applications such as aerospace and biomedical application for actuation (in Nitinol stents), sensing, vibration damping and impact absorption [4, 5, 2].

1.1.1 Morphology

The story behind the shape memory response resides in the crystalline phase transformation known as *martensitic phase transformation*, a solid to solid diffusionless (displacive) phase transformation where the lattice or molecular structure changes abruptly at some temperature. SMAs consist of two distinct phases. *Martensite* (M), the so-called low-temperature phase and the *austenite* (A),

or the high-temperature phase. Each of these phases posses different thermo-mechanical and cystallographic characteristics. Generally, austenite has cubic crystalline structure but martensite has the structure of monoclinic, tetragonal or orthorhombic. Transformations between these structures are rather displacive (without diffusion) and first-order. i.e. abrupt changes in lattice parameters. An important characteristic of the martensitic phase transformation is the microstructure it creates afterward. The lattice of high-temperature austenite phase (parent phase) has greater crystallographic symmetry than that of the low-temperature martensite phase (daughter phase)[3], Figure 1.3.

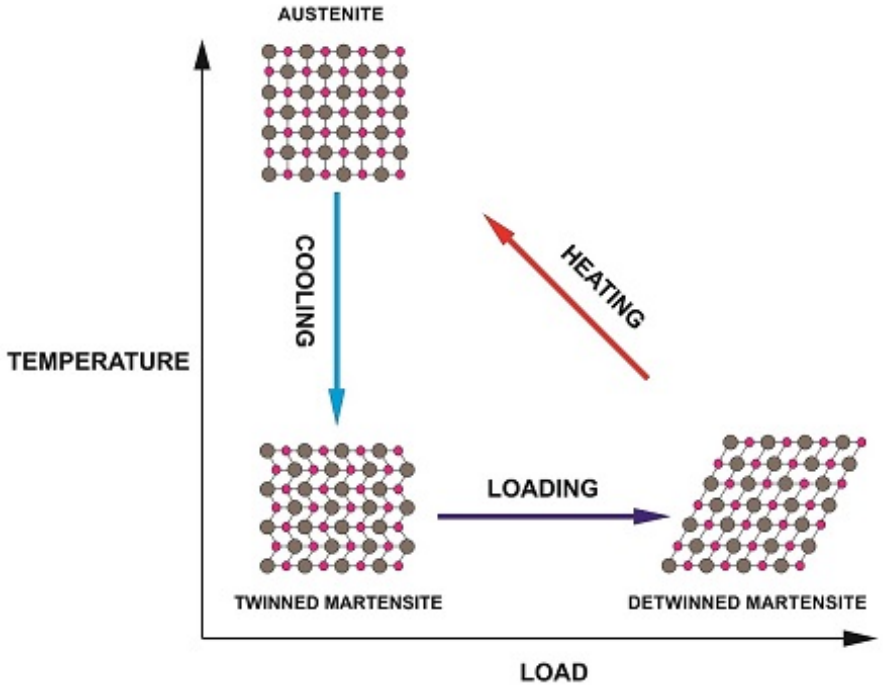

Figure 1.3: Martensitic phase transformation in SMAs.

Crystalline structure of martensite possess different orientation directions, which is called *variant*. Martensitic variants can assemble in two forms: *twinned* martensite (M^t), which is formed by a combination of "self-accommodated" martensitic variants [6], and detwinned martensite (or reoriented martensite) where (M^d) , a single specific variant is dominant.

There are four particular temperatures associated with phase transformations of SMAs, Figure 1.4. During cooling process, forward transformation (austenite to twinned martensite) begins at the *martensitic start-temperature* (M_s) . This transformation continues until the temperature decreases to *martensitic finish*

temperature (M_f). At this stage, the structure is in fully-twinned martensite and forward transformation is complete. When the temperature of the material is between M_s and M_f, applying mechanical load will result in detwinning the martensitic structure and reorienting a certain number of variants. Detwinning process will change the macroscopic shape, where deformed configuration will be preserved after unloading. An additional decrease in temperature (cooling) of SMA may result in further contraction (thermally), but nothing unusual happens (from the respect of shape change) [5]. Likewise, if we start heating the solid, the reverse transformation starts at *the austenitic start temperature* (A_s) and finishes at *the austenitic finish temperature* (A_f). The difference between transformation temperature from austenite to martensite and martensite to austenite is known as *hysteresis*. hysteresis may vary in different ranges of Celsius in different SMAs [3, 7].

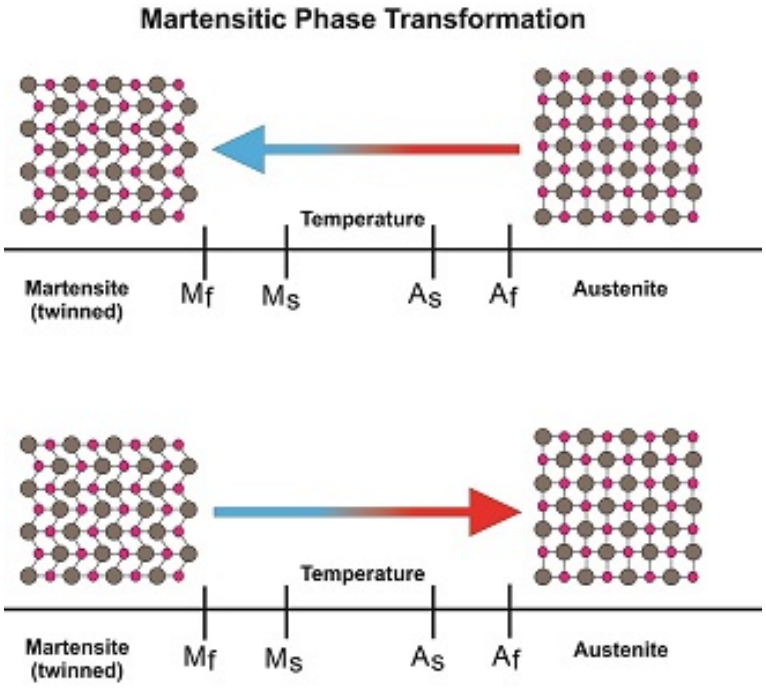

Figure 1.4: Transformation temperatures and crystallographic structure of SMAs.

1.1.2 Mechanical and Thermal Behaviors

Existence of two different phases and observable characteristics of martensitic phase transformation give rise to variety of mechanical and thermal behaviors in SMAs [8]. There are several numerical simulations to cover SMAs response

to uniaxial and thermal loading conditions. Some cases of these numerical simulations are:

1. Supermechanical
    - Pseudoelasticity.
    - Pseudoplasticity.
    - Existance of asymmetry in pseudoelastic response in tension and compression.
2. Superthermal
    - One-way shape memory effect (OWSME).
    - Cyclic Thermal loading under isobaric stress state.

1.1.2.1 Pseudoelasticity

Loading and unloading of SMA, when temperature is constant and above austenite finish ($\theta \gg A_f$), will result in stress-induced forward and reverse martensitic transformation. This behavior of SMAs is called **Pseudoelasticity** or **Superelasticity**. Figure 1.5 shows a "flag-like" strees-strain curve for superelastic behavior of SMAs under uniaxial isothermal loading conditions.

With the material being initially in austenite phase, loading from zero stress (point "0" in Figure 1.5) begins. After elastic loading path (point "1"), phase transformation from austenite to martensite starts (region "1-2"). Generally, it is limited with small hardening (rate independent) state. When transformation is complete (point "2") and martensitic phase is dominant (fully-martensitic phase), increasing stress can result in severe rehardening (region "2-3"). Note that, transformation strain or martensitic volume fraction (which is bounded by latter region) identifies the main factor of SMA modeling [9]. Point "4" corresponds the unloading, where region "4-5" represents the rapid reverse transformation from martensite (daughter phase) to austenite phase (parent phase). Note that, in real experiments, final phases always include some residual strain which indicates the fractions of martensite retained in the material.

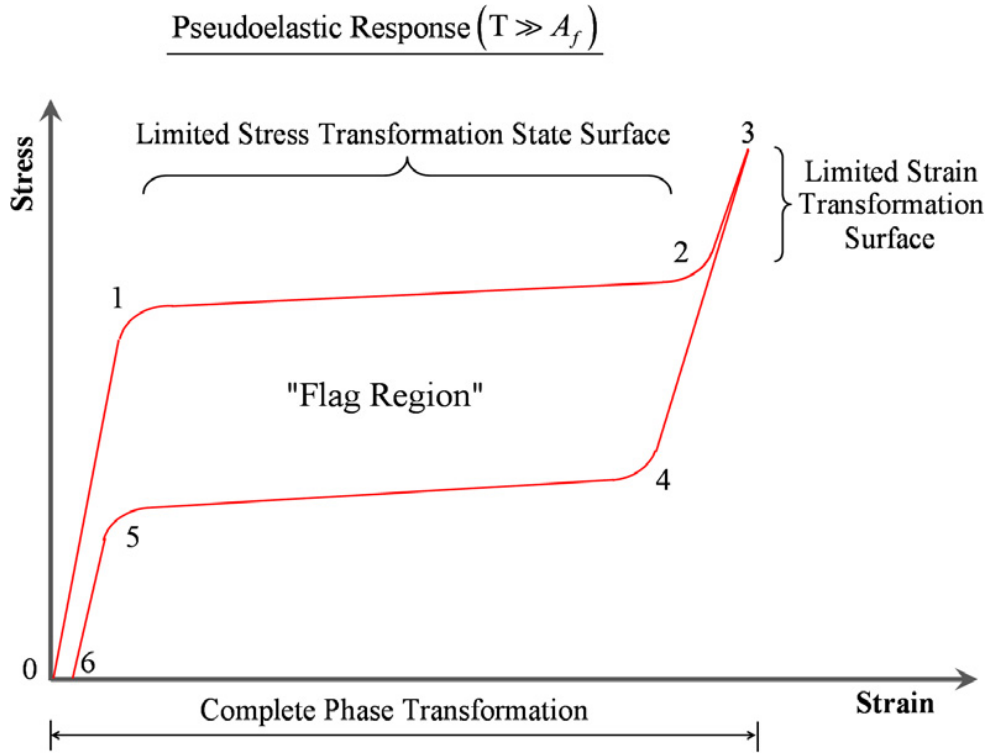

Figure 1.5: Schematic presentation of the ideal pseudoelasticity response of SMAs [2, 9].

1.1.2.2 Pseudoplasticity

Pseudoplasticity is the response of SMAs under uniaxial loading when temperature is below martensite finish temperature ($\theta \ll M_f$). After unloading, Low-temperature state leads to high percentage of residual strain as shown in Figure 1.6. Stress-induced transformation results in detwinning the initially twinned martensite structure. Although reversibility is not considered when the temperature is below M_f, SMAs can deform (reversibly) up to 8 percent strains.

Figure 1.7, demonstrates the evolutionary effect of an SMA material response under cyclic loading in the martensitic state. The amount of residual strain is high and can also reversibly deform about 5 times of regular steel.

1.1.2.3 One-way shape memory effect (OWSME)

In one-way shape memory effect, the material is initially in martensitic phase ($\theta \ll M_f$), subjected to loading and subsequent unloading (zero stress), its

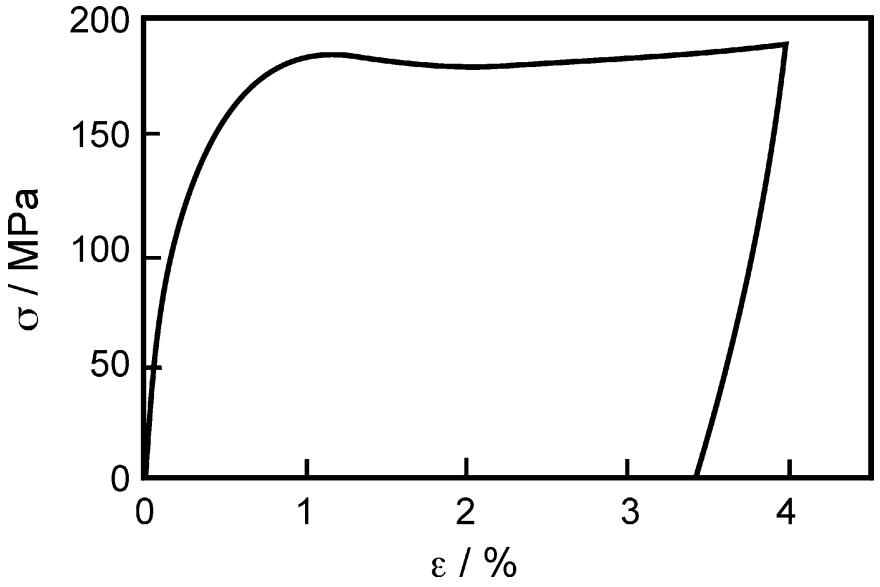

Figure 1.6: Stress–strain curve of pseudoplastic Ni-Ti [10]

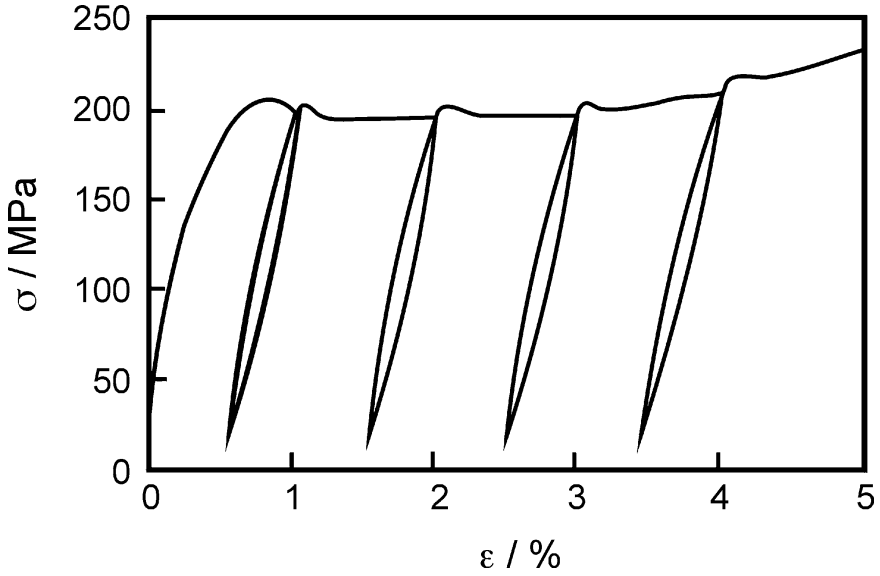

Figure 1.7: Pseudoplastic Ni-Ti under cyclic loading-unloading mechanical stress [10]

structure becomes detwinned martensite (by reorienting a certain number of variants). The detwinning process results in a macroscopic shape change [3]. By raising the temperature above the austenite finish temperate $\theta \gg A_f$, crystals of low-symmetry martensite phase tend to transform to the high-symmetry austenite phase, which results in complete shape recovery. Cooling back again results in twinned martensite with no shape change. Figure 1.8 demonstrates the details of OWSME and compares it with superelasticity response.

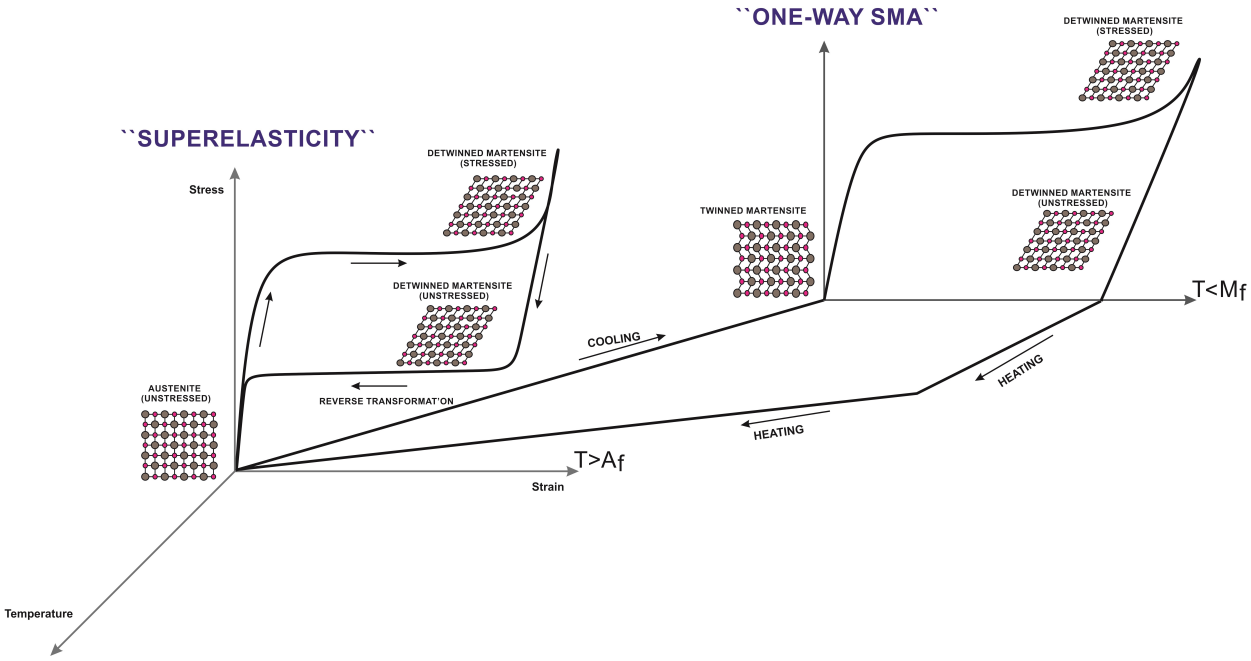

Figure 1.8: Pseudoelasticity response versus one-way shape memory effect.

1.1.2.4 Two-way shape memory effect (TWSME)

A Two-way shape memory metal can remember its configuration in both low and high temperatures (see Figure 1.2). In this case, some variants of the martensitic structure are also favored and does not adapt to the "self-accommodated" structure of the austenite [11]. This behavior can be observed due to repeated thermomechanical cycling along a specific loading path (training) [3] or the creation of precipitates in the material [12]. The symmetry and arrangement of point defects can be a possible reason for TWSME [13]. TWSME is not as common as OWSME because they deteriorate at high temperatures and are unstable in High-Temperature Shape Memory Alloys (HTSMA) systems (SMAs with transformation temperatures above 100^oC) [11].

1.2 Ni-Ti based SMAs

Nickel-Titanium alloy, also knows as Nitinol, is the most known shape memory alloys utilized in various applications. Exhibiting different behaviors of OWSME, TWSME and pseudoelasticity under different conditions make it suit-

able for commercial industrial applications. Corrosion resistance and biocompatibility also make it ideal for medical applications. Nowadays, compared to other SMAs (copper-based alloys, and iron-based alloys), thermo-mechanical characteristics, crystallography, and responses to heat treatment of this alloy are well understood. Moreover, there is a vast data about the variation of transformation temperatures with respect to composition changes [3], which facilitates the application of Nitinol in various fields of study.

Decisions on SMAs are not concentrated on shape memory functionality but also on utility features of specific SMA system. Another important point in highlighting SMAs, is the cost of production and manufacturing to get a desired shape memory effect at any temperature. The amount of knowledge we gained in this area contributes to handle these issues in the best way. Based on Alam et al. [14], price of Ni-Ti alloy has dropped from \$1000 DOLLAR/kg by the year 2000 to below \$200 DOLLAR/kg by the year 2015.

1.3 Literature Survey

Shape memory alloys (SMAs) hold a significant importance in different areas such as aeronautics, adaptive structures, oil/gas down-hole, and high-temperature automotive. Nowadays, researchers have already become well-aware of these applications and attempted to discover all the primary features of this specific material. Meanwhile, there is a growing effort to produce mathematical models in order to imitate the related behaviors in a precise manner. Research activities of shape memory alloys involve three main areas: (a) experimental research, (b) constitutive modeling, (c) analytical/computational work on the analysis of the boundary value problem of SMA structures and devices. Here, we will go over experimental work and modeling research done in the literature.

1.3.1 Experimental Research

Starting with the considerable work of Adharapurapu et al. [15], who conducted an experimental research on the effect of temperature on the stress-strain

response of Ni-Ti alloy (55.6%Ni by weight in alloy) at high strain rate and compared the results with quasi-static strain rate. Obtained results of this work is utilized to verify our constitutive model in the following chapters. Firstov et al. [16], observed behavior of an unusual intermetallic compound Ni_3Ta in order to investigate martensitic transformation, shape memory effect, transformation temperatures and hysteresis. They succeeded to determine the crystal structure parameters of austenite and martensite and hoped to open new perspectives for this specific material. Single crystal and polycrystalline Ni-Ti alloys were taken into consideration by Gall et al. [17], to find out the importance of crystallographic texture of shape memory alloys [18, 19]. Fatigue behaviors of single crystals are also investigated in this paper. In another experimental work, Lexcellent and Tobushi [20], investigated the stress-strain isothermal hysteresis loops of martensitic transformation in order to determine existence of two yield points for Ni-Ti shape memory alloys, One for forward transformation and another for reverse transformation. Tanaka et al. [21], took these results and generalized them to anisothermal conditions.

Liu et al. [22], conducted a valuable inspection on the asymmetry in tension and compression (ATC) under uniaxial loading conditions. Based on the observations in this work, behavior of Ni-Ti shape memory alloys under tension is different from its behavior under compression. We verified ATC behavior of our constitutive model with the findings of this paper. Next, three different single-crystal shape memory alloys C-Al-Be, Ni-Ti, and Cu-Zn-Al samples subjected to pure bending are studied experimentally and moment-curvature hysteresis loops are derived in a work by Rejzner et al. [23]. In this work, ATC is also considered in deriving non-linear differential equations for the motion of neutral plane. Under varying temperatures and different series of uniaxial loading conditions, an experimental research is conducted to investigate thermomechanical aspects of Ni-Ti by Shaw and Kyriakides [24]. Another experimental work, guided by Lissenden et al. [25], went over the time dependency of deformations in Titanium alloy. They carried out cyclic deformation tests under the stress-strain and rate controlled loading conditions. They were able to observe strain ratcheting for all of the cyclic tests.

Kockar et al. [26], investigated the effect of grain size on the thermo-mechanical cyclic stability of martensitic phase transformation of $Ni_{49.7}Ti_{50.3}$ shape memory alloy. For this purpose, they refined the grain size using equal-channel angular extrusion (ECAE) to 100-300 nm. They observed a considerable improvement in thermal stability by refining the grain size. In a more advanced work, Grabe and Bruhns [27], inspected the rate and viscous dependence of Ni-Ti subjected to two-dimensional uniaxial tension/torsion loading conditions. They further explored the relaxation behavior of Nitinol in this paper. Then, they extended their research to multiaxial experiments on the polycrystalline Ni-Ti shape memory alloy [28]. Within high range of temperatures, they investigated the path dependence of pseudoelasticy and one-way shape memory effect in both isothermal and temperature varying thermo-mechanical loading paths.

1.3.2 Constitutive Modeling

There are different approaches to model the behavior of SMAs. They can be primarily based on micro-mechanics, i.e. crystallography of SMA, macro-mechanics, i.e. phenomenological models of SMA, combination of micro and macro-mechanics, kinetics methods, and statistical mechanics. The development of numerical methods such as finite difference and finite element method (FEM) has led to preference for using continuum mechanics theory along with thermodynamic laws. Two essential theories of continuum mechanics are large strain theory and small strain theory of deformation. The reader is refered to [29, 30], in order to acquire knowledge about related concepts.

1.3.2.1 Models based on microscopic thermodynamic

Microscopic thermodynamic approach tends to model the microsrtructural features of SMAs such as growth of martensite grains, phase nucleation, motion of interfaces between two parent phases, and so forth. These models are derived using "Molecular Dynamics (MD)" theory or "Ginzburg-Landau Theory (GL)". Ginzburg-Landau theory is based on polynomial energy expression which is written in terms of strain and temperature. One of the pioneers in this modeling approach is Falk [31, 32]. His model can be counted as the first constitutive model of SMAs. Afterward, James and Ball [33], Barch and Kurumhansi [34], and Abeyarante [35] followed the same path and suggested some applicable models for SMAs.

Meanwhile, there exist some models based on molecular dynamics theory. In this theory, there is a system of finite numbers of particles which utilizes Newton's equations to describe the motion of every single particle of the system. In this category, models are mostly based on two different potential functions: embedded-atom-method (EAM) and Lennard-Jones (LJ). Lai and Liu [36], Ackland et al. [37], and Uehara and Tamai [38], are the examples of models on Ni-Ti SMA using EAM potential of MD theory. Within the framework of molecular dynamics, an alternative to EAM is Lennard-Jones potential. Kastner [39], investigated the evolutionary effect of martensitic phase transformation during a cyclic loading using LJ potential.

1.3.2.2 Macroscopic phenomenological models

Macroscopic models discuss phenomenological considerations of materials to model the related behaviors. There are different approaches associated with macroscopic modeling of materials;

- Theory of plasticity
- Statistical physics

One of the popular phenomenological models of SMAs, is the model of Tanaka

[40]. The model has utilized second law of thermodynamics in terms of Helmholtz free energy function. Temperature θ, uniaxial strain ϵ and martensitic volume fraction ξ are the only state variables. Within the scope of small strain deformation theory Barbarino et al. [41], and Bodaghi et al. [42], developed phenomenological models wherein, they considered two, scalar and directional, internal variables; martensitic volume fraction as scalar internal variable, and the preferred direction of oriented martensitic variants as directional internal variable. In a two-part paper by Patoor et al. [43], a study on the modeling of the single crystal and polycrystalline SMAs, dealing with the kinematics of the phase transformation and addressing different approaches for the development of the free energy and dissipation, is conducted in order to derive constitutive equations. Mechanism of two-way shape memory effect (TWSME) is investigated through the thermomechanical processes in a work by Wada and Liu [44, 45]. One of the recent applicable models, is the model of Hart et al. [46]. They assessed the effect of irrecoverable viscoplastic strains in SMAs; since, these accumulated plastic strains are the main event in SMAs subjected to high temperatures. Later in 2014, Chemisky et al. [47], extended this model to investigate the concepts of cyclic actuation behavior and transformation induced plasticity.

Another approach in macroscopic modeling is deriving models using a *thermodynamic potential*. In these models, microscopic, phenomenological, and physical consideration construct the frame of potential energies. These models mostly utilize the framework presented in Halphen and Nguyen [48]; with generalized standard materials including internal constraints. One of the most important models presented based on the thermodynamic potential is Zaki and Moumni (ZM) model [49, 50]. They considered two parameters in their modeling scope: first one is the martnesitic volume fraction and the other one is the martensite orientation strain tensor. They also explored the utility of their model by investigating the well-known ATC behavior [51]. Recently, they presented the numerical simulation of ZM model subjected to multiaxial non-proportional loading conditions in a conference proceeding of smart material and adaptive structures [52].

Within the range of finite strain theory of continuum media, Anand and Gurtin [53], have developed a three dimensional model for superelasticity response of Ni-Ti SMA. In their simulation, both isothermal and coupled thermomechanical response of superelasticity have been modeled within a framework that accounts for the thermodynamic laws. Following their work, Thamburaja [54] developed an isotropic-based constitutive model and Crystal-mechanics-based constitutive model for single-crystal and polycrystalline SMAs in his PhD thesis. Eight years later, he published a paper by taking Anand's large strain modeling algorithms [55], into account and finalized his model.

Similar to these works, there was a constitutive model to reproduce psudoelasticity behaviors of SMAs in finite strain by Aurricchio et al. [56]. They verified their isothermal model by applying it to simple typical structures like uniaxial test and four-point bending test. Barot et al. [57], developed a model for thermomechanical behavior of crystallizable shape memory polymers. They modeled original amorphous phase and semi-crystalline phase to capture shape-memory effect.

1.4 Aim of Thesis

In response of thermo-mechanical stimulus, shape memory alloys can demonstrate different characteristic behaviors. Due to this fact, they play a crucial role in different areas such as aeronautics, military, medical devices, actuators and etc. Nowadays, most scientists and researchers have already become well-aware of these applications and attempted to discover all the primary features of this specific material. Meanwhile, there is a growing effort to produce a mathematical model which is able to imitate the related behaviors in a precise manner.

In this thesis, we are motivated to develop a thermo-mechanically coupled phenomenological three-dimensional constitutive model to describe salient features of shape memory alloys, under different loading conditions. We utilize isotropic-based plasticity setting with standard balance laws, thermodynamic laws and

theory of microforce balance to develop our constitutive model. It is aimed to implement the constitutive model to ABAQUS/Implicit (2016) finite element program, by writing a user material subroutine (UMAT). Material parameters are taken and calibrated from experimental research existed in the literature. Our principal goal is to capture the pseudoelasticity response under uniaxial loading condition, and extend it to one-way shape memory effect under stress-strain-temperature cycling. Both isothermal and thermo-mechanically coupled conditions will be considered here.

1.5 Structure of the Work

Chapter 2, outlines the general theory of continuum mechanics and presents an entry path to the modeling concepts of SMAs.

In the framework of large-deformation continuum mechanics, *Chapter 3* is devoted to giving a detailed overview on the development of a thermo-mechanically coupled elastoplasticity theory to model the temperature dependency and transformation strain of SMAs. Development of theory based on the principle of virtual power is presented by investigating the macroscopic and microscopic force balance. Then, basic thermodynamic principles such as the balance of energy, and entropy imbalance are included in this chapter in order to develop the constitutive theory.

At the beginning of *Chapter 4*, material constants are tabled. Two-dimensional and three-dimensional geometry definitions and properties, required for finite element simulation, are explained thoroughly as well. Taking these finite element models into consideration, we carried out our coupled simulations. Results of pseudoelastic response along with one-way shape memory effect are presented graphically. Simulations of SMAs which are subjected to thermal cycling under uniaxial loading will be shown in this chapter, as well.

Chapter 5, is allotted to discuss the results and demonstrate the capability of our three-dimensional model in capturing the qualitative responses of SMAs.

CHAPTER 2

FINITE STRAIN THEORY OF CONTINUUM THERMODYNAMICS

Basic Fields

$\mathbf{x} = \chi(\mathbf{X}, t)$,	motion;
$\mathbf{F} = \nabla\chi, \quad J = \det\mathbf{F} > 0$,	deformation gradient;
$\mathbf{F} = \mathbf{F}^e\mathbf{F}^p$,	elastic-plastic decomposition of $\mathbf{F}$;
$\mathbf{F}^e, J^e = \det\mathbf{F}^e = J > 0$,	elsastic distortion;
$\mathbf{F}^p, J^p = \det\mathbf{F}^p = J = 1$,	inelsastic distortion;
$\mathbf{F}^e = \mathbf{R}^e\mathbf{U}^e$,	polar decomposition of $\mathbf{F}^e$;
$\mathbf{C}^e = \mathbf{F}^{eT}\mathbf{F}^e$,	elastic right Cauchy-Green tensor;
$\mathbf{T} = \mathbf{T}^T$,	Cauchy stress;
$\mathbf{T}_R = J\mathbf{T}\mathbf{F}^{-T}$,	Piola stress;
ψ,	free energy density per unit reference volume;
η,	entropy density per unit reference volume;
$\theta > 0$,	absolute temperature;
$\nabla\theta > 0$,	temperature gradient;
$\mathbf{q}$,	heat flux vector;
r	scalar heat supply;
ξ	total martensitic volume fraction;
$\dot{\xi}$	rate of the change of martensitic volume fraction

This chapter is devoted to giving a comprehensive view point on the development of finite strain theory of continuum mechanics. Such a theory, can be deployed on modeling and simulation of the thermo-mechanical response of various materials, including SMAs, used in different components and structures.

2.1 Large Deformation Theory

Large deformation theory (also called large strain or finite strain theory), is a theory of continuum mechanics that deals with large scale strains and rotations. While small deformation plasticity theories are widely used in the analysis and design of metal structures, such theories fall short in providing adequate basis for design against plastic-buckling and other structural instabilities, e.g, situations in which, although the strains may be small, the rotations are often large. Products made from ductile metals are often subjected to processing operations such as forging, rolling, extrusion and drawing, as well as finishing operations such as machining, and large plastic deformations are ubiquitous to such manufacturing processes. Also, a proper analysis of the stress and strain states associated with tips of cracks in structural components requires a theory of finite plasticity; for that reason, large deformation theories of plasticity form a strong *basis* for numerically based computational methods used for the design and analysis of processing operations.

Since even metals can undergo large elastic dilational changes under high pressures, such as under high velocity impact, it is important to formulate the theory within a thermodynamically consistent frame-indifferent description that allows both elastic and plastic deformations to be large[1].

[1] Notation: For a tensor $\mathbf{B}$, $\mathbf{B}^T$ denotes its transpose. tr$\mathbf{B}$ is the trace of tensor $\mathbf{B}$. The determinant of tensor $\mathbf{B}$ is det$\mathbf{B}$. For any tensor $\mathbf{B}$, sym$\mathbf{B} = 1/2(\mathbf{B} + \mathbf{B}^T)$, skw$\mathbf{B} = 1/2(\mathbf{B} - \mathbf{B}^T)$. $\mathbf{B}_0$ is the *deviatoric* part of $\mathbf{B}$ which is defined by $\mathbf{B}_0 = \mathbf{B} - 1/3(\text{tr}\mathbf{B})\mathbf{1}$. For the rest of details about tensor algebra, the reader is referred to Holzapfel [30].

2.2 Kinematics

Let us consider a homogeneous body $\mathbf{A}$ in reference (initial) configuration and take a material point $\mathbf{X}$ in $\mathbf{A}$ [2]. Motion of $\mathbf{A}$ can be identified as the one-to-one mapping of $\mathbf{x} = \chi(\mathbf{X}, t)$. On that account, *deformation gradient*, *velocity* and *velocity gradient* are given by:

$$\mathbf{F} = \nabla\chi, \quad \mathbf{v} = \dot{\chi}, \quad \mathbf{L} = \text{grad}\mathbf{v} = \dot{\mathbf{F}}\mathbf{F}^{-1}. \tag{2.2}$$

To model the inelastic response of the materials, we assume that the deformation gradient $\mathbf{F}$ may be decomposed as Kröner [60]:

$$\mathbf{F} = \mathbf{F}^{\mathrm{e}}\mathbf{F}^{\mathrm{p}}. \tag{2.3}$$

Accordingly, we assume:

$$J = \det\mathbf{F} \quad \text{with} \quad J^{\mathrm{e}} := \det\mathbf{F}^{\mathrm{e}} > 0,\ J^{\mathrm{p}} := \det\mathbf{F}^{\mathrm{p}} > 0,$$

so that $\mathbf{F}^e$ and $\mathbf{F}^p$ are invertible. Here, suppressing the argument:

- $\mathbf{F}^p(\mathbf{X})$ represents the inelastic part of deformation gradient which can be caused by different mechanisms, such as plastic distortion, damage or degradation mechanism, **phase deformation**, etc. This leads to carrying or pining the material point to a new local configuration.
- $\mathbf{F}^e(\mathbf{x})$ is responsible for the subsequent elastic deformation of material point $\mathbf{X}$. This elastic distortion includes stretching and rotation of the crystal lattices.

From now on, we refer to $\mathbf{F}^p$ and $\mathbf{F}^e$ as the *inelastic* and *elastic distortions*, respectively. By Eqs. 2.2 and 2.3,

$$\mathbf{L} = \mathbf{L}^{\mathrm{e}} + \mathbf{F}^{\mathrm{e}}\mathbf{L}^{\mathrm{p}}\mathbf{F}^{\mathrm{e}-1}, \tag{2.4}$$

with

$$\mathbf{L}^{\mathrm{e}} = \dot{\mathbf{F}}^{\mathrm{e}}\mathbf{F}^{\mathrm{e}-1}, \quad \mathbf{L}^{\mathrm{p}} = \dot{\mathbf{F}}^{\mathrm{p}}\mathbf{F}^{\mathrm{p}-1}. \tag{2.5}$$

[2] For further information about the concepts of *homogeneous body, reference configuration, current configuration, material point, etc.*, the reader is referred to Holzapfel [30], Lee [58], Gurtin et al. [59].

Hence, we define the total, elastic, and plastic stretching and spin tensors as follows:

$$\mathbf{D} = \mathrm{sym}\mathbf{L}, \quad \mathbf{W} = \mathrm{skw}\mathbf{L}, \tag{2.6}$$

so that

$$\mathbf{L} = \mathbf{D} + \mathbf{W},\ \mathbf{L}^e = \mathbf{D}^e + \mathbf{W}^e, \text{ and } \mathbf{L}^p = \mathbf{D}^p + \mathbf{W}^p.$$

The right and left polar decomposition of $\mathbf{F}$ are given by.

$$\mathbf{F} = \mathbf{RU} = \mathbf{VR}, \tag{2.7}$$

with

$$\mathbf{U} = \sqrt{\mathbf{F^T F}}, \quad \mathbf{V} = \sqrt{\mathbf{F F^T}}. \tag{2.8}$$

Where $\mathbf{R}$ is a rotation (proper orthogonal tensor), while $\mathbf{U}$ and $\mathbf{V}$ are right and left stretch tensors which are symmetric and positive definite tensors. Hence, we derive the logarithmic elastic strain tensor:

$$\mathbf{E}^e = \ln\mathbf{U}^e = \sum_{i=1}^{3} \mathbf{E}_i^e r_i^e \otimes r_i^e, \tag{2.9}$$

with principal values $\mathbf{E}_i^e = \ln\lambda_i^e$, where λ_i^e and r_i^e are the positive eigenvalues and eigenvectors of $\mathbf{U}^e$, respectively. The left and right Cauchy-Green tensors can also be defined as follows:

$$\mathbf{C} = \mathbf{U^2} = \mathbf{F^T F}, \quad \mathbf{B} = \mathbf{V^2} = \mathbf{F F^T}. \tag{2.10}$$

2.2.1 Incompressible, irrotational plastic flow

Here, we consider that the plastic flow follows two fundamental assumptions;

(i) First, *plastic flow* is incompressible;

$$J^{\mathrm{p}} = \det\mathbf{F}^p = 1 \quad \text{and} \quad \mathrm{tr}\mathbf{L}^p = 0, \tag{2.11}$$

hence,

$$J^e = J. \tag{2.12}$$

(ii) Second, under the circumstances in which SMA material may be idealized as isotropic, utilizing the Kroner [60] decomposition, we assume that the *martensitic transformation* is *irrotational* in the sense that:

$$\mathbf{W}^p = 0, \tag{2.13}$$

then, trivially, $\mathbf{L}^p \equiv \mathbf{D}^p$ and;

$$\dot{\mathbf{F}}^p = \mathbf{D}^p \mathbf{F}^p. \tag{2.14}$$

Thus, using Eqs. 2.14 2.4 2.5, and 2.14 we can conclude:

$$(\nabla \dot{\chi})\mathbf{F}^{-1} = \dot{\mathbf{F}}^e \mathbf{F}^{e-1} + \mathbf{F}^e \mathbf{D}^p \mathbf{F}^{e-1}. \tag{2.15}$$

2.3 Development of the theory based on the principle of virtual power

We take an arbitrary subregion $\mathbf{G}$ on the reference body $\mathbf{A}$, with n denoting the outward unit normal on the boundary $\partial\mathbf{G}$ of $\mathbf{G}$. Macroscopic motion of body leads to enforcing power on $\mathbf{G}$, which results in *macroscopic surface traction* $\mathbf{s}(\mathbf{n})$, measured per unit area in the reference body. Here, the body force, $\mathbf{b}$ accounts for inertia, which results in the fact that the following frame is inertial in a way:

$$\mathbf{b} = \mathbf{b}_0 - \rho \ddot{\chi}, \tag{2.16}$$

with $\mathbf{b}_0$ the non-inertial body force, and ρ_R the mass density in the reference configuration. Thus, *external power* can be written as:

$$W_{\text{ext}}(G) = \int_{\partial G} \mathbf{s}(\mathbf{n}) \cdot \dot{\chi} \text{da} + \int_G \mathbf{b} \cdot \dot{\chi} \text{dv}. \tag{2.17}$$

On that account, we assume that external power is consumed internally by an *elastic stress* $\mathbf{S}^e$ power-conjugate to $\dot{\mathbf{F}}^e$, and *plastic stress* $\mathbf{T}^p$ power-conjugate to $\mathbf{D}^p$. Thus, the *internal power* relation can be written as:

$$W_{\text{int}}(G) = \int_G (\mathbf{S}^e : \dot{\mathbf{F}}^{\mathbf{e}} + \mathbf{T}^p : \mathbf{D}^p) \text{dv}. \tag{2.18}$$

Since $\mathbf{D}^p$ is symmetric deviatoric, we can accordingly assume that $\mathbf{T}^p$ is *symmetric, deviatoric.*

2.3.1 Principal of virtual power

Let us assume some arbitrary fields as $\tilde{\dot{\chi}}$, $\tilde{\dot{\mathbf{F}}}^e$, and $\tilde{\mathbf{D}}^p$ which are consistent with Eq. 2.15, and consider that at a fix arbitrary chosen time χ, $\mathbf{F}^e$ (and hence $\mathbf{F}$ and $\mathbf{F}^p$ are known). Then, we require that [59]:

$$(\nabla\tilde{\dot{\chi}})\mathbf{F}^{-1} = \tilde{\dot{\mathbf{F}}}^e\mathbf{F}^{e-1} + \mathbf{F}^e\tilde{\mathbf{D}}^p\mathbf{F}^{e-1}. \tag{2.19}$$

Now let us define a *generalized virtual velocity* in order to be consistent with above Eq. 2.19:

$$\nu = (\tilde{\dot{\chi}}, \tilde{\dot{\mathbf{F}}}^e, \tilde{\mathbf{D}}^p)$$

Then, we write external, and internal power as:

$$\begin{aligned} W_{\text{ext}}(G,\nu) &= \int_{\partial G} \mathbf{s}(\mathbf{n})\cdot\tilde{\dot{\chi}} = \text{da} + \int_G \mathbf{b}\cdot\tilde{\dot{\chi}}\text{dv}, \\ W_{\text{int}}(G,\nu) &= \int_G (\mathbf{S}^e : \tilde{\dot{\mathbf{F}}}^{\mathbf{e}} + \mathbf{T}^p : \tilde{\mathbf{D}}^p)\text{dv}, \end{aligned} \tag{2.20}$$

for any part G, the *principle of virtual power* is the requirement for internal, and external power to be balanced:

$$W_{\text{int}}(G,\nu) = W_{\text{ext}}(G,\nu) \quad \text{for all virtual velocities } \nu. \tag{2.21}$$

2.3.2 Macroscopic force balance

In Eq. 2.21, we are free to choose any ν which is consistent with Eq. 2.20. So let us consider a case $\tilde{\mathbf{D}}^p \equiv 0$, in a way that:

$$\tilde{\dot{\mathbf{F}}}^e = \nabla\tilde{\dot{\chi}}\mathbf{F}^{p-1}. \tag{2.22}$$

With this definition of ν, Eq. 2.21 yields:

$$\int_{\partial G} \mathbf{s}(\mathbf{n})\cdot\dot{\chi}\text{da} + \int_G \mathbf{b}\cdot\dot{\chi}\text{dv} = \int_G (\mathbf{S}^e\mathbf{F}^{p-T}) : \nabla\tilde{\dot{\chi}}\text{dv}, \tag{2.23}$$

and by defining,

$$\mathbf{T}_R := \mathbf{S}^e\mathbf{F}^{p-T}, \tag{2.24}$$

and applying the divergence theorem results in:

$$\int_{\partial G} (\mathbf{s}(\mathbf{n}) - \mathbf{T}_R\mathbf{n}) \cdot \tilde{\dot{\chi}} \mathrm{da} + \int_G (\mathrm{Div}\mathbf{T} + b) \cdot \tilde{\dot{\chi}} \mathrm{dv} = 0.$$

As long as this relation must hold for all $\mathbf{G}$ then,

$$\mathbf{s}(\mathbf{n}) = \mathbf{T}_R(\mathbf{n}), \tag{2.25}$$

and the local macroscopic force balance:

$$\mathrm{Div}\mathbf{T}_R + \mathbf{b} = 0. \tag{2.26}$$

Besides, from the consequences of frame-indifference theory, and Eq. 2.24, we conclude that:

$$\mathbf{T}_R\mathbf{F}^T = \mathbf{F}\mathbf{T}_R^T. \tag{2.27}$$

Thus, $\mathbf{T}_R$ is considered as the classical *Piola stress*, and Eqs. 2.27, 2.26 indicate the local *macroscopic force, and moment balances* in the reference configuration [59]. Since the body force $\mathbf{b}$ accounts for inertia, so that Eq. 2.16 reduces to local balance law for linear momentum:

$$\mathrm{Div}\mathbf{T}_R + \mathbf{b}_0 = \rho\ddot{\chi}, \tag{2.28}$$

with $\mathbf{b}_0$ the non-inertial body force. Moreover, the Piola stress $\mathbf{T}_R$ is related to symmetric Cauchy stress $\mathbf{T}$ through:

$$\mathbf{T}_R = J\mathbf{T}\mathbf{F}^{-T}, \tag{2.29}$$

thus,

$$\mathbf{T} = J^{-1}\mathbf{T}_R\mathbf{F}^T. \tag{2.30}$$

considering Eq. 2.12, 2.24, and $\mathbf{F}^{eT} = \mathbf{F}^{p-T}\mathbf{F}^T$, Eq. 2.30, yields the Cauchy stress which is:

$$\mathbf{T} := J^{-1}\mathbf{S}^e\mathbf{F}^{eT}. \tag{2.31}$$

Note that:

$$\mathbf{S}^e = J^e\mathbf{T}\mathbf{F}^{e-T}, \tag{2.32}$$

and is the counterpart of the standard "first Piola stress" with respect to the intermediate space [59].

2.3.3 Microscopic force balance

Let us consider a generalized virtual velocity,

$$\tilde{\dot{\chi}} \equiv 0; \tag{2.33}$$

and arbitrarily choose the virtual field $\tilde{\mathbf{D}}^p$, and let the rate of virtual deformation tensor to be;

$$\tilde{\dot{\mathbf{F}}}^e = -\mathbf{F}^e \tilde{\mathbf{D}}^p, \tag{2.34}$$

consistent with Eq. 2.19. Therefore,

$$\mathbf{S}^e : \tilde{\dot{\mathbf{F}}}^e = -(\mathbf{F}^{eT}\mathbf{S}^e) : \tilde{\mathbf{D}}^p. \tag{2.35}$$

Further, let's define a *Mandel Stress* by,

$$\mathbf{M}^e := \mathbf{F}^{eT}\mathbf{S}^e = J\mathbf{F}^{eT}\mathbf{T}\mathbf{F}^{e-T}, \tag{2.36}$$

which is not symmetric generally. Then, considering our choice in Eq. 2.33, the external power vanishes, so that, by Eq.2.21, the internal power must also vanish, and satisfy,

$$W_{int}(G,\nu) = \int_G ((\mathbf{T}^p - \mathbf{M}^e) : \mathbf{D}^p)\, dv_R = 0.$$

Recent equation must satisfy for all G, and all tensors $\tilde{\mathbf{D}}^p$ (which are symmetric, and deviatoric), then it yields the *Microforce Balance*:

$$\mathrm{sym}_0\mathbf{M}^e = \mathbf{T}^p. \tag{2.37}$$

This microscopic balance denotes the interaction between internal forcese resulted from the elastic, and plastic response of the material [59].

2.4 Balance of energy. Entropy imbalance. Free-energy imbalance

Let,

- $\theta > 0$ denote the absolute temperature;

- ϵ and η denote the *internal energy* and *entropy densities*, both measured per unit volume of the reference configuration;
- $\mathbf{q}$ denote the *heat flux*, measured per unit area in the reference body;
- r denote the scalar value for heat supply, measured per unit volume in the reference body.

With above definitions, the *balance of energy* is:

$$\dot{\overline{\int_G \epsilon \mathrm{dv}}} = -\int_{\partial G} \mathbf{q} \cdot \mathbf{n} \mathrm{da} + \int_G r \mathrm{dv} + W_{\mathrm{ext}}(G), \tag{2.38}$$

while, *entropy imbalance* of the form (the *second law of thermodynamics*):

$$\dot{\overline{\int_G \eta \mathrm{dv}}} \geq -\int_{\partial G} (\frac{\mathbf{q}}{\theta}) \cdot \mathbf{n} \mathrm{da} + \int_G \frac{r}{\theta} \mathrm{dv}. \tag{2.39}$$

Therefore, based on equality of Eq 2.21, and since G is arbitrary, we may use Eq. 2.18 to acquire local forms of Eqs. 2.38 and 2.29 as follows,

$$\begin{aligned} \dot{\epsilon} &= -\mathrm{Div}\mathbf{q} + r + \mathbf{S}^e : \dot{\mathbf{F}}^e + \mathbf{T}^p : \mathbf{D}^p, \\ \dot{\eta} &\geq -\frac{1}{\theta}\mathrm{Div}\mathbf{q} + \frac{1}{\theta^2}\mathbf{q} \cdot \nabla\theta + \frac{r}{\theta}. \end{aligned} \tag{2.40}$$

Let,

$$\psi := \epsilon - \theta\eta, \tag{2.41}$$

present the *Helmholtz free energy* per unit volume of the reference body. Then, by Eq. 2.40, the *local free-energy imbalance* becomes:

$$\dot{\psi} + \eta\dot{\theta} + \frac{1}{\theta}\mathbf{q} \cdot \nabla\theta - \mathbf{S}^e : \dot{\mathbf{F}}^e - \mathbf{T}^p : \mathbf{D}^p \leq 0. \tag{2.42}$$

Note that two conjugate tensors of stress and deformation rate pair $(\mathbf{S}^e, \dot{\mathbf{F}}^e)$ in Eq. 2.42, are not frame-invariant. Thus, we introduce a new stress tensor in order to use in the balance of internal energy and free energy imbalance. Recall from Eq. 2.32 that,

$$\mathbf{S}^e = J\mathbf{T}\mathbf{F}^{e-T}. \tag{2.43}$$

Let us introduce a new stress relation:

$$\mathbf{T}^e := \mathbf{F}^{e-1}\mathbf{S}^e = J\mathbf{F}^{e-1}\mathbf{T}\mathbf{F}^{e-T}, \tag{2.44}$$

the symmetric $\mathbf{T}^e$ represents a second Piola stress. Note that, Mandel stress defined in Eq. 2.36 becomes:

$$\mathbf{M}^e = \mathbf{C}^e\mathbf{T}^e. \tag{2.45}$$

It is straightforward to show that:

$$\mathbf{S}^e : \dot{\mathbf{F}}^e = \frac{1}{2}\mathbf{T}^e : \dot{\mathbf{C}}^e, \tag{2.46}$$

thus, the internal power is:

$$\frac{1}{2}\mathbf{T}^e : \dot{\mathbf{C}}^e + \mathbf{T}^p : \mathbf{D}^p. \tag{2.47}$$

Then, the energy imbalance 2.40 may be written as:

$$\dot{\epsilon} = -\text{Div}\mathbf{q} + r + \frac{1}{2}\mathbf{T}^e : \dot{\mathbf{C}}^e + \mathbf{T}^p : \mathbf{D}^p. \tag{2.48}$$

While the free energy imbalance 2.42 becomes;

$$\dot{\psi} + \eta\dot{\theta} + \frac{1}{\theta}\mathbf{q} \cdot \nabla\theta - \frac{1}{2}\mathbf{T}^e : \dot{\mathbf{C}}^e - \mathbf{T}^p : \mathbf{D}^p \leq 0. \tag{2.49}$$

We note that following fields are frame-invariant:

$$\psi, \quad \eta, \quad \theta, \quad \mathbf{C}, \quad \mathbf{M}^e, \quad \mathbf{D}^p. \tag{2.50}$$

2.5 Rate-dependency of the theory

From the balance of microforce law, we consider that Mandel stress is related to flow direction using a rate dependent function of Y, through:

$$\mathbf{M}_0^e = Y(d^p, S)\mathbf{N}^p, \tag{2.51}$$

where $d^p = |\mathbf{D}^p|$ and S is positive scalar hardening variable. We assume that Y function has the form:

$$Y(d^p, S) \longrightarrow g(d^p)Y(S). \tag{2.52}$$

Therefore, Eq 2.51 becomes:

$$\mathbf{M}_0^e = g(d^p)Y(S)\mathbf{N}^p. \tag{2.53}$$

It is assumed that the rate sensitivity function $g(d^p)$ satisfies $g(0) = 0$, and it is monotonically increasing function of d^p, which is *invertible*. We take absolute value of the Eq. 2.53,

$$\frac{|\mathbf{M}_0^e|}{Y(S)} = g(d^p), \tag{2.54}$$

which is invertible to:

$$d^p = g^{-1}\left(\frac{|\mathbf{M}_0^e|}{Y(S)}\right) \longrightarrow d^p = f\left(\frac{|\mathbf{M}_0^e|}{Y(S)}\right). \tag{2.55}$$

Here, special form of *power-law function* is going to be used. This function has important utility in characterizing experimental data. From the power-law function:

$$g(d^p) = \left(\frac{d^p}{d^0}\right)^m, \tag{2.56}$$

where, $m > 0$, is a rate-sensitivity parameter. thus:

$$d^p = d_0\left(\frac{|\mathbf{M_0^e}|}{Y(S)}\right)^{1/m}. \tag{2.57}$$

From the flow rule we already know that $\mathbf{N}^p = \dfrac{\mathbf{M}_0^e}{|\mathbf{M_0^e}|}$. Taking this into consideration, we conclude:

$$\mathbf{D}^p = d_0\left(\frac{|\mathbf{M_0^e}|}{Y(S)}\right)^{1/m}\frac{\mathbf{M}_0^e}{|\mathbf{M_0^e}|}. \tag{2.58}$$

This indicates how rate-dependency affects the evolution of *phase transformation.*

CHAPTER 3

DERIVATION OF THE CONSTITUTIVE MODEL FOR NI-TI SHAPE MEMORY ALLOY

In this section, we summarize our continuum mechanics-based constitutive model for Ni-Ti shape memory alloy, capable of representing martenstic phase transformation, pseudoelasticity, and one-way shape memory effect. The related framework is similar in spirit to the isotropic plasticity-based theory of Anand and Gurtin [53].

We recall some points from the previous chapter and extend it to constitutive modeling of Ni-Ti SMA. To construct the constitutive theory, using the standard notation of modern continuum mechanics, we recall that the deformation gradient $\mathbf{F}$, maps *referential* segments $\mathbf{dX}$ to segments $\mathbf{dx} = \mathbf{FdX}$ in the *deformed* configuration. The list of the governing variables in the constitutive model are:

(i) The Helmholtz free energy per unit *reference* volume, ψ.

(ii) The Cauchy stress tensor, $\mathbf{T}$.

(iii) The total deformation gradient tensor, $\mathbf{F}$ with $\det\mathbf{F} > 0$.

(iv) The absolute temperature, θ.

(v) The martensitic phase change tensor, $\mathbf{F}^p$ wit $\det\mathbf{F}^p > 0$. It denotes the cumulative inelastic strain due to martensitic phase deformation.

(vi) The elastic tensor (no martensitic phase transformation), $\mathbf{F}^e$ with $\det\mathbf{F}^e > 0$. It describes the elastic stretches that give rise to the Cauchy stress $\mathbf{T}$.

From the theory of Kröner [60] and Lee [58], the elastic distortion tensor is given by $\mathbf{F}^e = \mathbf{F}\mathbf{F}^{p-1}$.

(vii) The total martensite volume fraction, ξ with $0 \leq \xi \leq 1$

3.1 Kinematics of the theory

Here, $\mathbf{x}$ indicates the position vector of the material point in the current configuration. The velocity vector, which is time derivative of the position vector with respect to time becomes, $\mathbf{v} = \dot{\mathbf{x}}$. The derivative of the deformation gradient tensor with respect to time is:

$$\dot{\mathbf{F}} \equiv \text{grad}\mathbf{v} = \mathbf{L}\mathbf{F}, \tag{3.1}$$

where $\mathbf{L}$ denotes the *total velocity gradient*. Using the definition $\mathbf{F} = \mathbf{F}^e\mathbf{F}^p$, total velocity gradient can be represented as:

$$\mathbf{L} = \mathbf{L}^e + \mathbf{F}^e\mathbf{L}^p\mathbf{L}^{p-1}, \tag{3.2}$$

where $\mathbf{L}^e = \dot{\mathbf{F}}^{\mathbf{e}}\mathbf{F}^{\mathbf{e-1}}$ and $\mathbf{L}^p = \dot{\mathbf{F}}^p\mathbf{F}^{p-1}$ represent the elastic and inelastic part of velocity gradients, respectively. Let's consider the polar decomposition of deformation tensor, $\mathbf{F} = \mathbf{R}\mathbf{U}$, and drive the logarithmic elastic strain tensor:

$$\mathbf{E}^e = \ln\mathbf{U}^e = \sum_{i=1}^{3} \mathbf{E}_i^e r_i^e \otimes r_i^e, \tag{3.3}$$

with principal values $\mathbf{E}_i^e = \ln\lambda_i^e$, where λ_i^e and r_i^e are the positive eigenvalues and eigenvectors of $\mathbf{U}^e$, respectively. Our formulation is based on two important assumptions: (1) referred to the work of Anand and Gurtin [61], the inelastic velocity gradient, $\mathbf{L}^p$ is taken to be *spinless* i.e. $\text{skw}\mathbf{L}^p = \mathbf{W}^p = \mathbf{0}$, and (2) the martensitic phase transformation is isochoric (volume preserving) [62] i.e. $\mathbf{L}^p$ is purely *deviatoric*.

By taking these points into consideration from previous chapter, we generalize the work of Sun and Hwang [62] to a large-strain setting and express the inelastic velocity gradient as:

$$\mathbf{L}^p = k(1 + a\phi)\sum_{i=1}^{2} \dot{\xi}_i.\dot{\mathbf{N}}_i \tag{3.4}$$

Here, $\dot{\xi}_1 \geq 0$ and $\dot{\xi}_2 \leq 0$ is the rate of change in the martensite volume fraction. In forward transformation, $\dot{\xi}_1 > 0$, whereas in reverse transformation $\dot{\xi}_2 < 0$. $k > 0$ is a constant of proportionality, a is a dimensionless scalar parameter, calibrated from experimental studies and controls the degree of asymmetry in tension-compression. Following the work of Orgeas and Favier [63], ϕ denotes the third stress-invariant measure, i.e. J_3, with the value of $0 \leq \phi \leq 1$. Before the martensitic phase transformation, martensitic volume fraction is zero ($\xi = 0$), then at end of transformation it becomes one ($\xi = 1$). For forward and reverse transformation, we define $\mathbf{N}_1$ and $\mathbf{N}_2$ as the *flow direction*. The flow direction tensors $\mathbf{N}_i$, are traceless and symmetric, i.e. $\mathbf{N}_i = \mathbf{N}_i^T$ and $\mathrm{tr}\mathbf{N}_i = 0$. From the work of Auricchio et al. [56], martensitic volume fraction change is taken to be:

$$\dot{\xi} = \sum_{i=1}^{2} \dot{\xi}_i = \dot{\xi}_1 + \dot{\xi}_2. \tag{3.5}$$

In Eq. 3.4, we will further enforce, $|\mathbf{N}_i| = \epsilon_T$, where ϵ_T is the experimentally determined constant which defines transformation strain of austenite-martensite phase transformation.

Inspired by the work of Sun and Hwang and Boyd and Lagoudas [62, 64], it has been deducted that reverse transformation is restricted by the history of forward transformation. In another words, martensite-austenite transformation is the recovery of the austenite-martensite transformation. Therefore, with $\mathbf{N}_1$ in hand, we can derive the reverse transformation flow direction $\mathbf{N}_2$ as:

$$\mathbf{N}_2 = \epsilon_T \left[\frac{\mathbf{B}}{|\mathbf{B}|} \right] \quad \text{with} \quad \dot{\mathbf{B}} = \mathbf{L}^p.$$

Here, $\mathbf{B}$ is a tensor defined in the same configuration as $\mathbf{F}^p$, i.e. relaxed configuration [65].

3.2 Micro-force balance

A micro-force system is a system that describes forces which perform work associated to martensitic phase transformation. This system consists of:

- The micro-traction vector, $\mathbf{c}$ - per unit area - *reference* configuration

- The scalar *internal* micro-force, π_{int} - per unit volume - *reference* configuration
- The scalar *external* micro-force, π_{ext}, - per unit volume - *reference* configuration

Following the work of Gurtin [66], we can write the corresponding micro-force balance equation based on the above micro-force systems, as:

$$\int_{\partial\Re} \mathbf{c}\cdot\mathbf{n}\,\mathrm{d}A + \int_{\Re} \pi_{\text{ext}}\,\mathrm{d}V = \int_{\Re} \pi_{\text{int}}\,\mathrm{d}V. \tag{3.6}$$

Using divergence theorem and localization of the results of Eq. 3.6:

$$\mathrm{Div}\,\mathbf{c} - \pi_{\text{int}} + \pi_{\text{ext}} = 0, \tag{3.7}$$

while $\mathbf{c}, \pi_{int}$ and π_{ext} are the functions of martensite volume fraction ξ and martensitic transformation rate $\dot{\xi}$, respectively:

$$\mathbf{c} = \hat{\mathbf{c}}(\xi,\dot{\xi}), \quad \pi_{\text{int}} = \hat{\pi}_{\text{int}}(\xi,\dot{\xi}), \quad \pi_{\text{ext}} = \hat{\pi}_{\text{ext}}(\xi,\dot{\xi}).$$

3.3 Balance of linear momentum

The balance of linear momentum is written as:

$$\int_{\partial\Re} \mathbf{T}_R\mathbf{n}\,\mathrm{d}A + \int_{\Re} \mathbf{b}\,\mathrm{dV} = \mathbf{0}. \tag{3.8}$$

Where $\mathbf{T}_R = (\mathrm{det}\mathbf{F})\mathbf{T}\mathbf{F}^{-T}$, is the first Piola-Kirchhoff stress tensor and $\mathbf{b}$ the macroscopic body force vector per unit volume in reference configuration (which includes inertial forces as well). Applying divergence law and localizing the results in Eq. 3.8 yields:

$$\mathrm{Div}\,\mathbf{T}_R + \mathbf{b} = 0. \tag{3.9}$$

3.4 Balance of angular momentum

The balance of angular momentum is given by:

$$\int_{\partial\Re} \mathbf{y}\times\mathbf{T}_R\mathbf{n}\,\mathrm{dA} + \int_{\Re} \mathbf{y}\times\mathbf{b}\,\mathrm{dV} = 0. \tag{3.10}$$

Using divergence theorem and localizing the results of Eq. 3.10, while using Eq. 3.9, result in:

$$\mathbf{T}_R\mathbf{F}^T = \mathbf{F}\mathbf{T}_R^T. \tag{3.11}$$

Substituting $\mathbf{T}_R = (\det\mathbf{F})\mathbf{T}\mathbf{F}^{-T}$ into Eq. 3.11 results in $\mathbf{T} = \mathbf{T}^T$ i.e. the Cauchy stress is symmetric.

3.5 Balance of energy

The balance of energy (first law of thermodynamics) is defined as:

$$\int_{\partial\Re}\left[\mathbf{T}_R\mathbf{n}\cdot\mathbf{v} + (\mathbf{c}\cdot\mathbf{n})\dot{\xi} - \mathbf{q}\cdot\mathbf{n}\right]\mathrm{dA} + \int_{\Re}(\mathbf{b}\cdot\mathbf{v} + \pi_{\mathrm{ext}}\dot{\xi} + r)\mathrm{dV} = \frac{d}{dt}\int_{\Re}\epsilon\mathrm{dV}, \tag{3.12}$$

while, ϵ is the internal energy per unit reference volume. Here $\mathbf{q}$ is the heat flux vector measured per unit area in the *reference* configuration and r is the heat supply per unit reference volume. While using Eqs. 3.1, 3.7 and 3.9, applying divergence theorem and localizing results yield:

$$\mathbf{T}_R\mathbf{F}^T\cdot\mathbf{L} + \mathbf{c}\cdot\nabla\dot{\xi} + \pi_{\mathrm{int}}\dot{\xi} - \mathrm{Div}\mathbf{q} + r = \dot{\epsilon}. \tag{3.13}$$

Substituting $\mathbf{T}_R = (\det\mathbf{F})\mathbf{T}\mathbf{F}^{-T}$, Eqs. 3.2, 3.3 and 3.7 into Eq. 3.13 while using the result of Eq. 3.11 and assuming that the external micro-force vanishes i.e. $\pi_{ext} = 0$,

$$\mathbf{T}^*\cdot\dot{\mathbf{E}}^e + \bar{\mathbf{T}}\cdot\mathbf{L}^p + \mathbf{c}\cdot\nabla\dot{\xi} + (\mathrm{Div}\mathbf{c})\dot{\xi} - \mathrm{Div}\mathbf{q} + r = \dot{\epsilon}, \tag{3.14}$$

where

$$\mathbf{T}^* = (\det\mathbf{F})\mathbf{F}^{e-1}\mathbf{T}\mathbf{F}^{e-T} \quad \text{and} \quad \bar{\mathbf{T}} = \mathbf{C}^e\mathbf{T}^*, \tag{3.15}$$

denote frame-invariant measures of stress. Note that $\mathbf{T}^*$ is symmetric whereas $\bar{\mathbf{T}}$ is generally not symmetric.

3.6 Entropy imbalance

The second law of thermodynamics (entropy imbalance) is written as:

$$\frac{d}{dt}\int_{\Re}\eta\mathrm{dV} \geqslant \int_{\partial\Re} -\frac{\mathbf{q}}{\theta}\cdot\mathbf{n}dA + \int_{\Re}\frac{r}{\theta}\mathrm{dV}. \tag{3.16}$$

When η is the entropy per unit reference volume. Applying divergence law and localizing the results, yield:

$$\dot{\eta}\theta + \text{Div}\mathbf{q} - \frac{\mathbf{q}}{\theta} \cdot \nabla\theta - r \geqslant 0. \tag{3.17}$$

Then, lets define Helmholtz free energy per unit reference volume, ψ, as:

$$\psi = \epsilon - \eta\theta \rightarrow \dot{\psi} = \dot{\epsilon} - \dot{\eta}\theta - \eta\dot{\theta}. \tag{3.18}$$

Here, we use the functional form of the free energy density [67], thus;

$$\psi = \hat{\psi}(\mathbf{E}^e, \xi, \theta) \rightarrow \dot{\psi} = \frac{\partial\psi}{\partial\mathbf{E}^e} \cdot \dot{\mathbf{E}}^e + \frac{\partial\psi}{\partial\xi}\dot{\xi} + \frac{\partial\psi}{\partial\theta}\dot{\theta}. \tag{3.19}$$

Substituting Eqs. 3.19 and 3.18, into Eq. 3.14 results in,

$$\left(\mathbf{T}^* - \frac{\partial\psi}{\partial\mathbf{E}^e}\right) \cdot \dot{\mathbf{E}}^e - \left(\eta + \frac{\partial\psi}{\partial\theta}\right)\dot{\theta} + \Gamma = \dot{\eta}\theta, \tag{3.20}$$

where

$$\Gamma \equiv \bar{\mathbf{T}} \cdot \mathbf{L}^p + (\text{Div}\mathbf{c})\dot{\xi} - \frac{\partial\psi}{\partial\xi}\dot{\xi} - \text{Div}\mathbf{q} + r. \tag{3.21}$$

Substitution of Eq. 3.20 into Eq. 3.17 results in the *dissipation inequality*:

$$\left(\mathbf{T}^* - \frac{\partial\psi}{\partial\mathbf{E}^e}\right) \cdot \dot{\mathbf{E}}^e - \left(\eta + \frac{\partial\psi}{\partial\theta}\right)\dot{\theta} + \Pi \geqslant 0, \tag{3.22}$$

where

$$\Pi \equiv \bar{\mathbf{T}} \cdot \mathbf{L}^p + (\text{Div}\mathbf{c})\dot{\xi} - \frac{\partial\psi}{\partial\xi}\dot{\xi} - \frac{\mathbf{q}}{\theta} \cdot \nabla\theta. \tag{3.23}$$

From rational thermodynamic arguments, inequality 3.22 results in;

$$\mathbf{T}^* = \frac{\partial\psi}{\partial\mathbf{E}^e}, \quad \text{and} \quad \eta = -\frac{\partial\psi}{\partial\theta}. \tag{3.24}$$

Eqs. 3.24_1, and 3.24_2 are the constitutive equations for the stress, entropy and the micro-traction vector, respectively.

3.7 Fourier's law and phase transformation criteria

From Eq. 3.24, we can drive the *reduced dissipation inequality* from inequality Eq. 3.22:

$$\Pi \equiv \bar{\mathbf{T}} \cdot \mathbf{L}^p + (\text{Div}\mathbf{c})\dot{\xi} - \frac{\partial\psi}{\partial\xi}\dot{\xi} - \frac{\mathbf{q}}{\theta} \cdot \nabla\theta \geqslant 0. \tag{3.25}$$

Here Π represents the total dissipation and it is always non-negative. By assuming each dissipative mechanism to be strongly dissipative [53], substituting Eqs. 3.4, 3.5 into Eq. 3.25, yields:

$$f_1\dot{\xi_1} > 0 \quad \text{whenever} \quad \dot{\xi}_1 \neq 0, \tag{3.26}$$

where $f_1 \equiv k(1+a\phi)[sym\bar{\mathbf{T}}_0 \cdot \mathbf{N}_1] + \text{Div}\mathbf{c} - \dfrac{\partial\psi}{\partial\xi}$, is the driving force for *forward* transformation,

$$f_2\dot{\xi_2} > 0 \quad \text{whenever} \quad \dot{\xi}_2 \neq 0, \tag{3.27}$$

where $f_2 \equiv k(1+a\phi)[sym\bar{\mathbf{T}}_0 \cdot \mathbf{N}_2] + \text{Div}\mathbf{c} - \dfrac{\partial\psi}{\partial\xi}$, is the driving force for *reverse* transformation. Finally,

$$-\frac{\mathbf{q}}{\theta} \cdot \nabla\theta > 0 \quad \text{whenever} \quad \nabla\theta \neq \mathbf{0}. \tag{3.28}$$

It is assumed that above inequalities are all obeyed at all times in a way that reduced dissipation inequality 3.25 is currently satisfied. Under the assumption of *rate-dependence*, in order to satisfy inequality of Eq. 3.26, we choose an expression for f_1, as follows:

$$f_1 = f_{c1} \quad \text{whenever} \quad \dot{\xi}_1 > 0, \tag{3.29}$$

where $f_{c1} = \hat{f}_{c1}(\theta) > 0$ denotes the *critical resistance to forward transformation;*

$$f_2 = -f_{c2} \quad \text{whenever} \quad \dot{\xi}_2 < 0, \tag{3.30}$$

where $f_{c2} = \hat{f}_{c2}(\theta) > 0$ denotes the *critical resistance to reveres transformation* As it is already known, we can assume that the material obeys Fourier's law of heat conduction, we take:

$$\mathbf{q} = -k_{th}\nabla\theta. \tag{3.31}$$

Where $k_{th} = \hat{k}_{th}(\xi,\theta) > 0$ represents the coefficient of thermal conductivity. To satisfy Eq. 3.28 $k_{th} = \hat{k}_{th}(\xi,\theta) > 0$, but for simplicity, we will assume that coefficient of thermal conductivity is constant at all times regardless of martensitic transformation and temperature.

3.8 Constitutive function of the free energy density

Free-energy density used in our constitutive modeling is taken to contain the free-energy of conventional shape-memory alloy, Helm [67]. We consider the free energy per unit *reference* volume, ψ to be in separable form as follows:

$$\psi = \psi^e(\mathbf{E}^e, \theta) + \psi^\xi(\xi, \theta) + \psi^\theta(\theta), \tag{3.32}$$

where

$$\begin{aligned}
&\psi^e(\mathbf{E}^e, \theta) = \mu|\mathbf{E}_0^e|^2 + \kappa(\mathrm{tr}\mathbf{E}^e)^2 - 3\kappa\alpha_{th}(\theta - \theta_0)(\mathrm{tr}\mathbf{E}^e), \\
&\psi^\xi(\xi, \theta) = \frac{\lambda_T}{\theta_T}(\theta - \theta_T)\xi + \frac{1}{2}\mathbf{h}\xi^2, \\
&\psi^\theta(\theta) = c(\theta - \theta_0) - c\theta log(\frac{\theta}{\theta_0}).
\end{aligned} \tag{3.33}$$

Here, ψ^e denotes the classical thermo-elastic free energy density with $\mu = \hat{\mu}(\xi, \theta)$, $\kappa = \hat{\kappa}(\xi, \theta)$ and $\alpha_{th} = \hat{\alpha}_{th}(\xi, \theta)$ represent the shear modulus, bulk modulus and the coefficient of thermal expansion, respectively.

The martensitic phase transformation energy is defined by ψ^ξ, where λ_T and θ_T represent the *latent* heat released/absorbed (units of energy per unit volume) during phase transformation, and the *phase equilibrium* temperature, respectively. Moreover, the energetic interaction coefficient, h has units of energy per unit volume.

Purely thermal portion of the free energy is denoted by ψ^θ with $c = \hat{c}(\xi, \theta)$, being the specific heat per unit *reference* volume. In this thesis, we follow the modeling assumption presented by Abeyaratne and Knowles [35]. They suppress the dependence of μ, κ, α_{th} and c on the martensite volume fraction and temperature, and consider them as constants.

3.9 Constitutive function of the stress and entropy

Substituting Eq. 3.32 into Eq. 3.24_1, results in the stress equation:

$$\mathbf{T}^* = 2\mu\mathbf{E}_0^e + \kappa\left[\mathrm{tr}\mathbf{E}^e - 3\alpha_{th}(\theta - \theta_0)\right]\mathbf{1}. \tag{3.34}$$

Further, Substituting Eq. 3.32 into Eq. 3.24_2, results in the entropy density for constitutive equation:

$$\eta = c\log(\theta/\theta_0) + 3\kappa\alpha_{th}(\mathrm{tr}\mathbf{E}^e) - (\lambda_T/\theta_T)\xi. \tag{3.35}$$

3.10 Flow direction $\mathbf{N}_1$ and the J_3 parameter

Since, we assumed that material is elastically-isotropic, we can conclude from stress equation 3.34, that $\mathbf{E}^e$ and $\mathbf{T}^*$ are co-axial. Thus, the stress tensor $\bar{\mathbf{T}} \equiv \mathbf{C}^e\mathbf{T}^*$ is also symmetric. Using this result and substituting Eqs. 3.32 and 3.34 into the equation of driving force for phase transformation results in:

$$f_1 = k(1+a\phi)(\bar{\mathbf{T}}_0 \cdot \mathbf{N}_1) - \frac{\lambda_T}{\theta_T}(\theta - \theta_T) - h\xi, \tag{3.36}$$

$$f_2 = k(1+a\phi)(\bar{\mathbf{T}}_0 \cdot \mathbf{N}_2) - \frac{\lambda_T}{\theta_T}(\theta - \theta_T) - h\xi. \tag{3.37}$$

Substituting Eq. 3.36 into Eq. 3.29, while $\dot{\xi} \neq 0$ (forward transformation), yields:

$$k(1+a\phi)(\bar{\mathbf{T}}_0 \cdot \mathbf{N}_1) = \frac{\lambda_T}{\theta_T}(\theta - \theta_T) + h\xi + f_{c1}(sign(\dot{\xi}_1)). \tag{3.38}$$

In order to satisfy Eq. 3.38, we take:

$$(\epsilon_T)^2[k(1+a\phi)]\bar{\mathbf{T}}_0 = \left\{\frac{\lambda_T}{\theta_T}(\theta - \theta_T) + h\xi + f_{c1}(sign(\dot{\xi}_1))\right\}\mathbf{N}_1. \tag{3.39}$$

Since $|\mathbf{N}_1| = \epsilon_T$. Taking the magnitude of both sides of Eq. 3.39 results in:

$$\mathbf{N}_1 = \epsilon_T\left\{\frac{\bar{\mathbf{T}}_0}{|\bar{\mathbf{T}}_0|}\right\} \longrightarrow f_1 = \bar{\sigma}\epsilon_T(1+a\phi) - \frac{\lambda_T}{\theta_T}(\theta - \theta_T) - h\xi, \tag{3.40}$$

where $\bar{\sigma} = \kappa|\bar{\mathbf{T}}_0|$ represents an *equivalent stress*. Following the work of Orgeas and Favier [68], the J_3 parameter is then given by:

$$\phi = \sqrt{6}\left[\mathbf{N}_1 \cdot \mathbf{N}_1^2\right](\epsilon_T)^{-3}.$$

3.11 Flow rule

During forward transformation i.e. $\dot{\xi}_1 \neq 0$ and $\dot{\xi}_2 = 0$, we get:

$$\epsilon_T(1+a\phi)\dot{\xi}_1 \equiv \sqrt{2/3}|\mathrm{sym}\mathbf{L}^p| \longrightarrow k = \sqrt{3/2} \quad and \quad \bar{\sigma} = \sqrt{3/2}|\bar{\mathbf{T}}_0|.$$

As mentioned above, $\bar{\sigma}$ is *equivalent* tensile stress or *Mises* stress. Thus, the final form of the *flow rule* i.e. the inelastic strain-rate is then given by:

$$\mathbf{L}^p = \sqrt{3/2}(1 + a\phi) \sum_{i=1}^{2} \dot{\xi}_i \mathbf{N}_i. \tag{3.41}$$

3.12 Related criteria for the driving forces and phase transformation rates

The criteria for the driving forces f_1 and f_2 are defined as follows:
$f_1 \leqslant f_{c1}$ for $0 \leqslant \xi < 1$,
$f_2 \geqslant -f_{c2}$ for $0 < \xi \leqslant 1$,

- for $\xi = 1$: the driving force for forward transformation is defined for all values of f_1.
- for $\xi = 0$: the driving force for forward transformation is defined for all values of f_2.

Conditions for phase transformation between martensite and austenite in a *rate-dependent* theory, are:

- Conditions for elastic range: If $f_1 \neq f_{c1}$, then $\dot{\xi} = 0$. If $f_2 \neq -f_{c2}$, then $\dot{\xi} = 0$
- Forward transformation: If $0 \leqslant \xi < 1$ and $f_1 = f_{c1}$, then
$$\dot{\xi}_1(\dot{\overline{f_1 - f_{c1}}}) = 0. \tag{3.42}$$
- Reverse transformation: If $0 < \xi \leqslant 1$ and $f_2 = -f_{c2}$, then
$$\dot{\xi}_2(\dot{\overline{f_2 - f_{c2}}}) = 0. \tag{3.43}$$
- End conditions: If $\xi = 1$ and $f_1 = f_{c1}$, then $\dot{\xi} = 0$. If $\xi = 0$ and $f_2 = -f_{c2}$, then, $\dot{\xi}_2 = 0$.

Eqs. 3.42 and 3.43, represent the *consistency conditions* for forward and reverse phase transformation, receptively [65]. These consistency conditions are used to determine the transformation rates $\dot{\xi}_1$ and $\dot{\xi}_2$.

3.12.1 Balance of energy

Substituting Eqs. 3.31, 3.32, 3.34 and 3.35 into Eq. 3.20 gives:

$$\bar{\mathbf{T}}_0 \cdot \mathbf{L}^p - \frac{\lambda_T}{\theta_T}(\theta - \theta_T)\dot{\xi} + k_{th}(\nabla^2\theta) + r = \dot{\eta}\theta. \tag{3.44}$$

Taking the time-derivation of Eq. 3.35, yields:

$$\dot{\eta} = (\frac{c}{\theta})\dot{\theta} + 3\kappa\alpha_{th}(\mathrm{tr}\dot{\mathbf{E}}^e)\theta - (\lambda_T/\theta_T)\dot{\xi}. \tag{3.45}$$

By substituting Eqs. 3.5, 3.41 and 3.45 into Eq. 3.44, we can drive evolution equation for temperature as follows:

$$c\dot{\theta} = k_{th}(\nabla^2\theta) + (\lambda_T/\theta_T)\theta\dot{\xi} - 3\kappa\alpha_{th}(\mathrm{tr}\dot{\mathbf{E}}^e)\theta + \sum_{i=1}^{2} f_i\dot{\xi} + r. \tag{3.46}$$

CHAPTER 4

RESULTS OF FINITE ELEMENT SIMULATIONS

Previous chapter was concerned with the comprehensive explanation on the related energy functions, evolution algorithms, and the constitutive equations. In this chapter, we are planning to present numerical simulations to demonstrate the capability of our fully coupled 3-D modeling framework. On that account, simulations of following cases will be considered under uniaxial stress/strain-controlled loading conditions,

- Pseudoelastic response,
- Asymmetry in tension and compression of pseudoelastic response,
- Pseudoplastic response,
- One-way shape memory effect,
- Stress-controlled and strain-controlled thermal cycling.

Note that UMAT (user material subroutine) has been written and implemented to FE program ABAQUS® (ABAQUS/Implicit, 2016) to perform the simulations.

Throughout this chapter, basic assumptions have been made towards the final model of polycrystalline Ni-Ti SMA: that material constants such as thermal expansion, heat capacity and, bulk modulus are independent of austenite-martensite crystal structure. Likewise, concluded from isotropic-plasticity theory, the material is assumed to be isotropic. It should be mentioned that none

of these simplifications/assumptions play a critical role in presenting the constitutive model and they can be disregarded straighforwardly. Our presented results in this chapter, reveals the admissibility of these assumptions.

4.1 Material constants and geometry definitions

In this thesis, we did not carry out any kind of experimental research to provide material parameters for Ni-Ti alloy. We only aimed to demonstrate the *qualitative features* of the *mechanically rate-dependent* model. For this reason, all material parameters are taken from Thamburaja and Anand [69], who conducted experiments on the textured sheet of the polycrystalline Ni-Ti alloy. Table 4.1, represents the values for all of these parameters which are used in our model. Based on the assumption taken by Abeyaratne and Knowles [35], we will not consider the dependence of material parameters on the martensitic volume fraction and temperature, and keep them constant throughout the phase transformation. Thus, estimated transformation temperatures are as follows:

$$\theta_{ms} = 251.3\,\mathrm{K}, \theta_{mf} = 213.0\,\mathrm{K}, \theta_{as} = 260.3\,\mathrm{K}, \theta_{af} = 268.5\,\mathrm{K}.$$

Table 4.1: Material parameters of polycrystalline rod Ni-Ti [69].

$\mu = 23.31\,\mathrm{GPa}$	$\kappa = 60.78\,\mathrm{GPa}$	$\alpha_{th} = 10 \times 10^{-6}\,\mathrm{K}^{-1}$	$\epsilon_T = 0.046$
$a = 0.13$	$h = 0\,\mathrm{J/m^3}$	$c = 2.08\,\mathrm{MJ/Km^3}$	$K_{th} = 18\,\mathrm{W/mK}$
$\theta_T = 255.8\,\mathrm{K}$	$\lambda_T = 97\,\mathrm{MJ/m^3}$	$f_c = 7.8\,\mathrm{MJ/m^3}$	$r = 0\,\mathrm{W/m^3}$

For implementing our model into finite element simulation, first of all, *a thermo-mechanically-coupled continuum 3-D brick single-element, C3D8RT*, is taken into account as shown in Figure 4.1(a)[1].

In a sense, elaboration of phenomenological models is in pledge of targeting complicated geometries. Thus, in order to look deeper into the roots of written implicit code and investigate the rate of convergence, from ABAQUS documentations [70], we hired *a 2-D plane strain, 4-node bilinear hybrid with temperature*

[1] *C3D8RT*, is a general purpose temperature-displacement continuum linear brick element, with reduced integration (1 integration point).

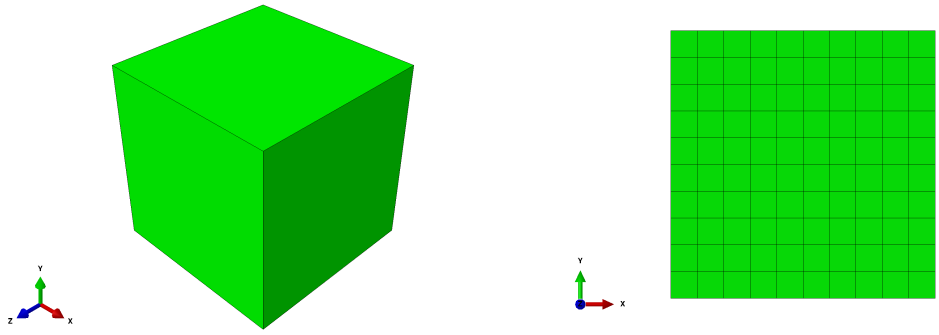

(a) (b)

Figure 4.1: Schematic view of geometric finite element mesh with thermo-mechanically-coupled element type, (a) single three-dimensional C3D8RT element. (b) plane strain CPE4HT element.

and displacement degrees of freedom, CPE4HT [70], element type. This 2-D multi-element finite element model contributes to verify the validity of framework as well. Figure. 4.1(b) demonstrates the schematic view of 2-D finite element model.

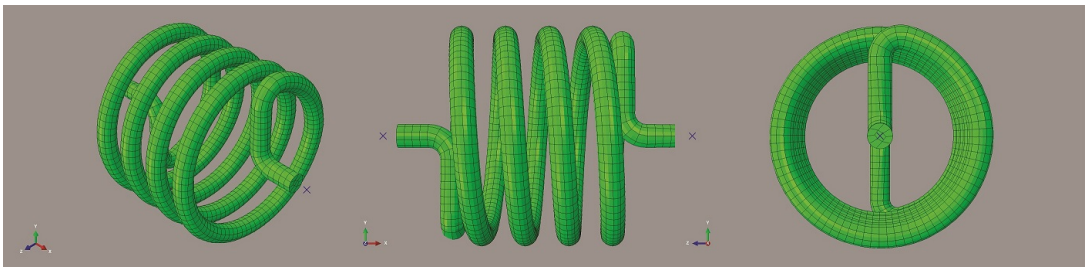

Figure 4.2: Geometric finite element mesh of a four-coil SMA actuator.

Finally, taking the importance of application of SMA helical actuators in electrical and aerospace industries into consideration, we implemented a SMA helical spring finite element model, as illustrated in Figure 4.2. Accordingly, the geometric variables of spring coil are indicated in Table 4.2. Helical spring finite element model can play an important role in evaluating of SMA model under different conditions of geometric complexity and can also be a clear 3-D model to enable a precise demonstration of one-way memory effect. For the purpose of integrity in results, a refined mesh of total 3920 C3D20RHT elements (*20-node thermally coupled brick, triquadratic displacement, trilinear temperature, hybrid,*

linear pressure, reduced integration, three-dimensional [70]), were applied for the analysis.

In the upcoming sections, we are about to deal with the set of key state variables which introduce major features of SMAs; that is to construct a reliable scope for our constitutive model.

Table 4.2: Geometric parameters of the helical SMA spring [71].

Variables	Values
Number of helix, n	4
Mean coil Diameter, D_m (mm)	12.7
Inside coil Diameter, D_i (mm)	11.2
outside coil Diameter, D_o (mm)	14.2
wire Diameter, d (mm)	1.5
Pitch height,P (mm)	2.8
Pitch angle, α (deg)	4.014

In the most following experimental plots, we are aimed at carrying out a qualitative comparison between experimental findings of literature and ideal behavior of SMAs simulated by numerical analysis. Due to this reason, we ignore the quantitative arguments as stress plateau numbers, strain amounts and so forth.

4.2 Pseudoelasticity response

Pseudoelasticity is the initial departure point for characterizing the reliability of every SMA model. In that account, we conducted a simple tension and compression test on the derived SMA constitutive model calibrated with material parameters stated in the Table 4.1. Subjected to tensile stress, boundary conditions are applied in a way that the resultant shapes for both 3-D and 2-D finite element models are deformed as exhibited in Figures 4.3(a) and 4.3(b), respectively.

At the beginning of deformation, material is fully-austenitic, ($\theta = 298 > \theta_{af}$). Critical resistances of forward-reverse transformation are supposed to be equal and independent of temperature (for the all numerical simulations). An isothermal simulation of 2-D and 3-D finite element models performed under both stress

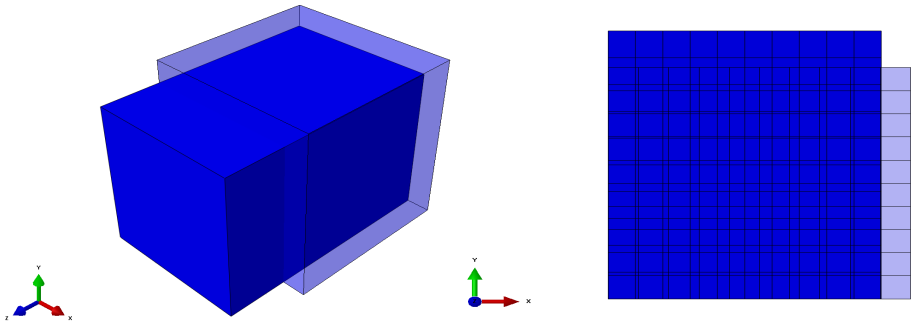

(a) (b)

Figure 4.3: Deformed and undeformed shape of finite element mesh at the end of loading and unloading step, (a) 3-D Geometry (b) 2-D plain strain geometry. Shaded parts are the initial configurations.

and strain-controlled loading conditions. As shown in Figure 4.4(a) and 4.4(b), material initially behave elastically. Crystallization of martensite leads to subsequent perfect plasticity $h = 0$. At the end of phase transformation, material begins to harden elastically since we have a fully martensitic structure. As unloading begins, reverse transformation from martnesite to austenite takes place and the the material navigate in the same manner as forward transformation, (See Figure. 4.4(a) 4.4(b)). Results of the experimental analysis taken from Huo and Muller [72], are also presented in the 4.4(c). It can be inferred from the graphs that the plastic deformation is directly delivered by the advance and retreat of the martensitic volume fraction. Martensitic phase transformation is induced just at the presence of mechanical loading. In the experimental plots of Figure 4.4 and in most subsequent figures, we are aimed at carrying out a qualitative comparison between experimental findings and ideal behavior of SMAs simulated by numerical analysis. Due to this reason, we ignore the quantitative arguments as stress plateau numbers, strain amounts and so forth.

In order to observe the formation of hysteresis loop during pseudoelastic behavior, the following simulation conducted under isothermal loading condition. The sample is subjected to tensile stress in a way that each cycle ends before the completion of martensitic phase transformation. This repeats also for the reverse transformation in the opposite manner. In the experiment conducted by Huo and Miller [72], hysteresis loop derived for this cyclic loading. It is concluded

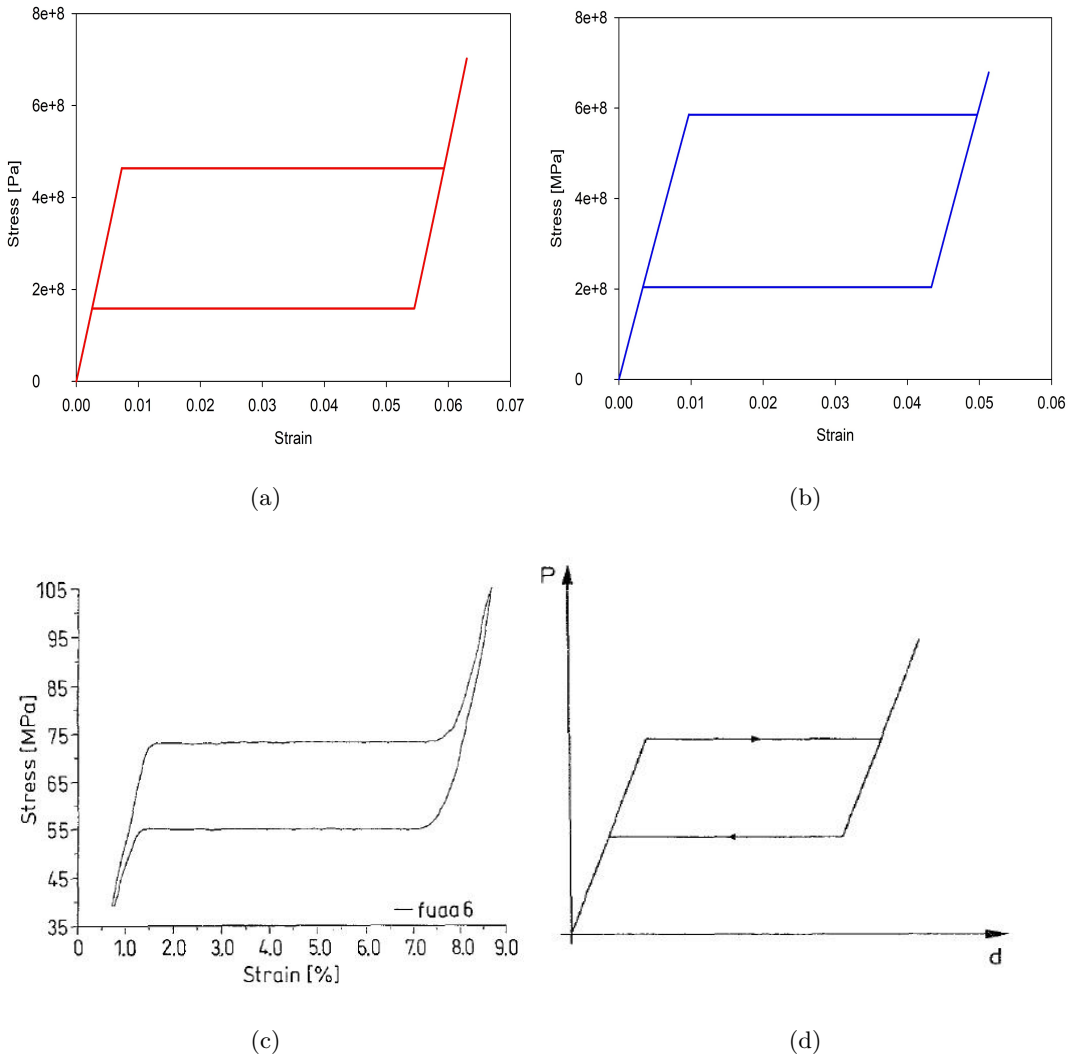

Figure 4.4: Pseudoelastic response of Ni-Ti SMA under (a) uniaxial tension, (b) uniaxial compresssion. (c) Experimental results of pseudoelasticity obtained from Huo and Muller [72]. (d) Ideal behavior expected by Huo and Muller [72].

that AB line is region that full thermodynamic equilibrium take place for all internal and external state variables and driving force of phase transformation is zero. As it is illustrated in 4.5(a), the derived constitutive model can produce this phenomenon in a satisfying manner.

4.2.1 Hardening effect

Another analysis conducted while energetic interaction coefficient is set to- $h = 2 \times 10^4\, J/m^3$. In the spirit of modeling inelastic materials, h coefficient

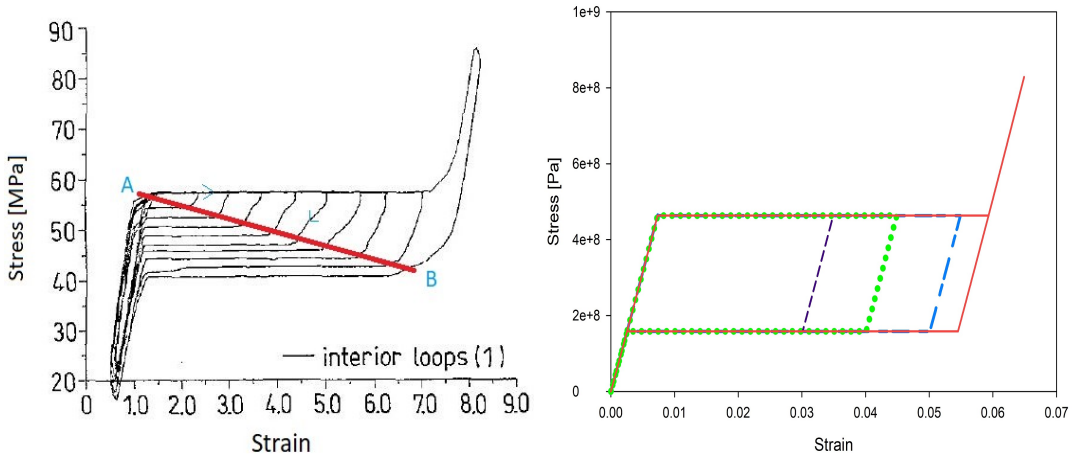

(a) (b)

Figure 4.5: Formation of hysteresis loop due to partial cyclic loading-unloading. (a) Results of experimental findings by Huo and Muller [72] for CuZnAl SMA. (b) Results of numerical simulation of related behavior.

is responsible for the hardening behavior of the material (if there is any). It should be mentioned that we have isotropic kind of hardening here. Figure 4.6 indicates the result of this analysis.

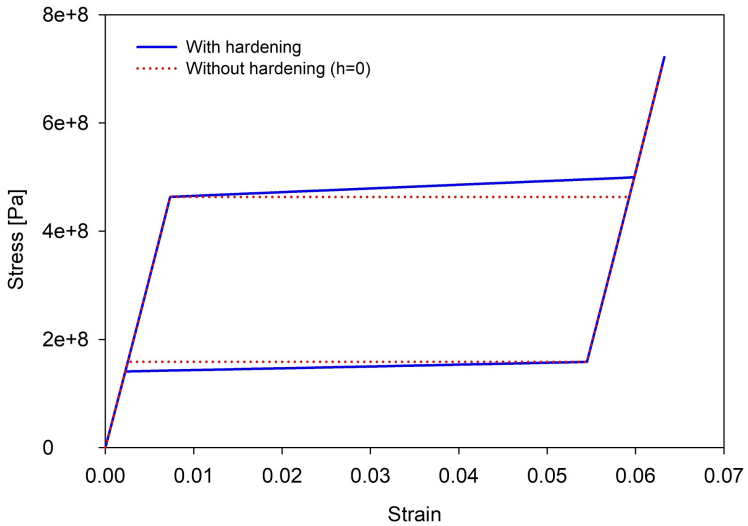

Figure 4.6: Comparison of pseudoelasticity response with hardening and without hardening.

4.2.2 Temperature effect in isothermal analysis

In another investigation of pseudoelasticity behavior, we performed a simulation with two different ambient temperatures ($\theta_0 = 288\,K \,\&\, \theta_0 = 308\,K$). With the material parameters calibrated with respect to Table 4.1, simple isothermal tension loading-unloading analysis is conducted with our model. As illustrated in the plots 4.7(a), and 4.7(b), the required stress to induce forward and reverse transformation increases by increasing ambient temperature (i.e. critical stress is dependent linearly on temperature). In another words, critical stress increases from 400MPa to 580MPa as temperature increases from 288K to 308K. However, the area of hysteresis loop remains unchanged due to the fact that hysteresis is independant of temperature in pseudoelasticity. Unchenged hysteresis loop results in equal transformation strains for all temperatures. This is inferred from the stress exploitation of thermo-elastic portion of energy function. All of these results take place in a same manner as experimental findings of Huo and Muller [72] and Tanaka et al. [21].

4.2.3 Strain-rate effect

Amount of the strain rate-dependency of the model will be taken into consideration in this section. Figure 4.8(a) demonstrates three different pseudoelastic responses conducted with various strain-rates under thermo-mechanically coupled conditions. Increasing strain-rate exhibits different trends in stress-strain response of pseudoelastic behavior:

- A larger hardening happens in forward transformation.
- A larger softening happens in reverse transformation.
- Hysteresis loop gets wider (dissipation increases).

The causes for the observed trends are as follows: in the low strain-rate $m = 1 \times 10^4$, simulation behaves in a nearly isothermal way, i.e. martensitic phase transformation occurs in a constant stress plateaus. However, by increasing

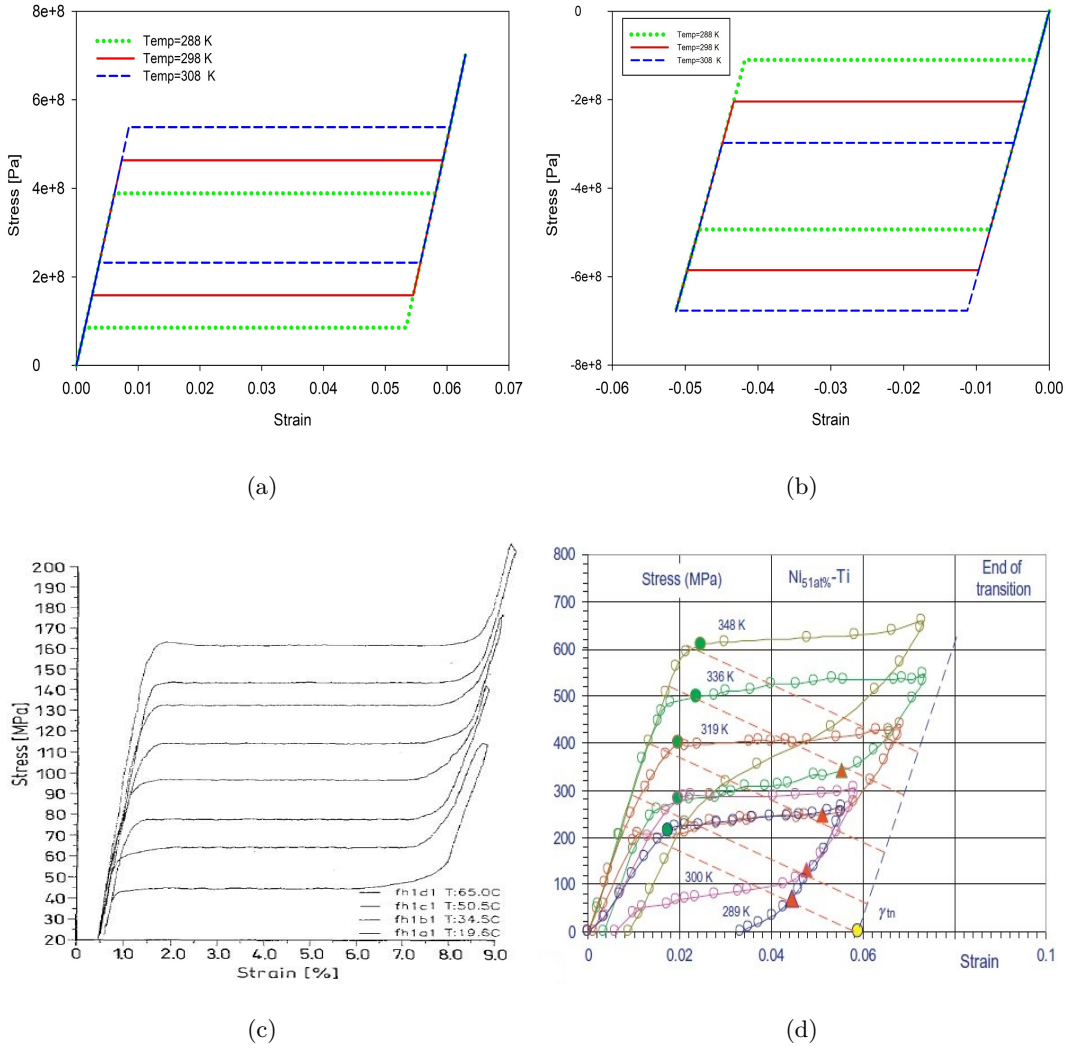

Figure 4.7: Stress-strain plot of the pseudoelastic response under different temperatures, (a) tension loading, (b) compression loading. (c) Experimental results of Huo and Muller[72] for CuZnAl, (d) experimental results of Tanaka et al [21] for Ni-Ti

deformation-rate, simulation leads to non-isothermal results. Analysis' contours demonstrate generation of temperature field in high strain-rates. That being so, generated temperature causes hardening during phase transformation.

4.2.4 Fully-coupled simulation

Finally, fully-coupled thermo-mechanical behavior of our model is exhibited in Figure 4.9(a). In the forward transformation, since the generated heat energy due to mechanical dissipation and release of latent heat do not leave the spec-

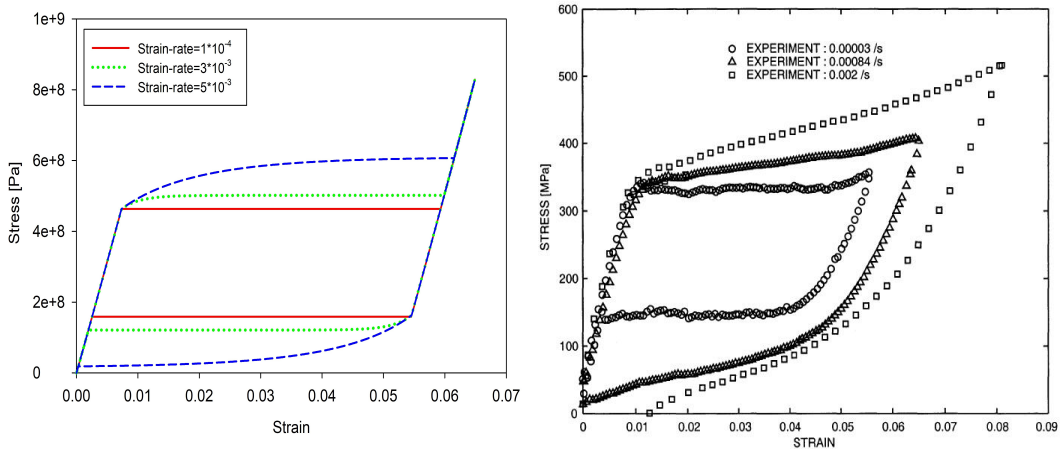

(a) (b)

Figure 4.8: Strain-rate effect on the stress-sttrain curve of pseudoelasticity. (a) Numerical simulation results. (b) Experimental results [15].

imen quickly (through conduction and convection), temperature-time response indicates 39 K increase in one cycle of uniaxial loading-unloading tensile stress. This increased temperature causes hardening in stress-strain curve during analysis, Figure 4.9(b). However, in the reverse transformation, absorbed heat due to the phase transformation (latent heat) exceeds the heat generated by mechanical dissipation, thus, this results in decreasing the temperature of specimen with respect to ambient temperature to 302 K. This is the decrease in temperature which leads to softening of material in reverse transformation, Figure 4.9(b). Total increase of 4 K in temperature is the output of the mechanical dissipation in one cycle of uniaxial loading-unloading tensile stress.

As mentioned previously, coupled behavior of the model emerges from the evolution equation for the temperature (Eq 3.46), which is perfectly embedded into UMAT code. The detailed step by step algorithm is presented in appendix A.

4.3 Asymmetry in tension and compression (ATC)

Literature of shape memory alloys are full of cases which discuss the asymmetry in tension and compression (ATC) of SMAs [22][15][73]. To investigate this behavior in Ni-Ti SMA, the numerical stress-strain curves are plotted repeatedly

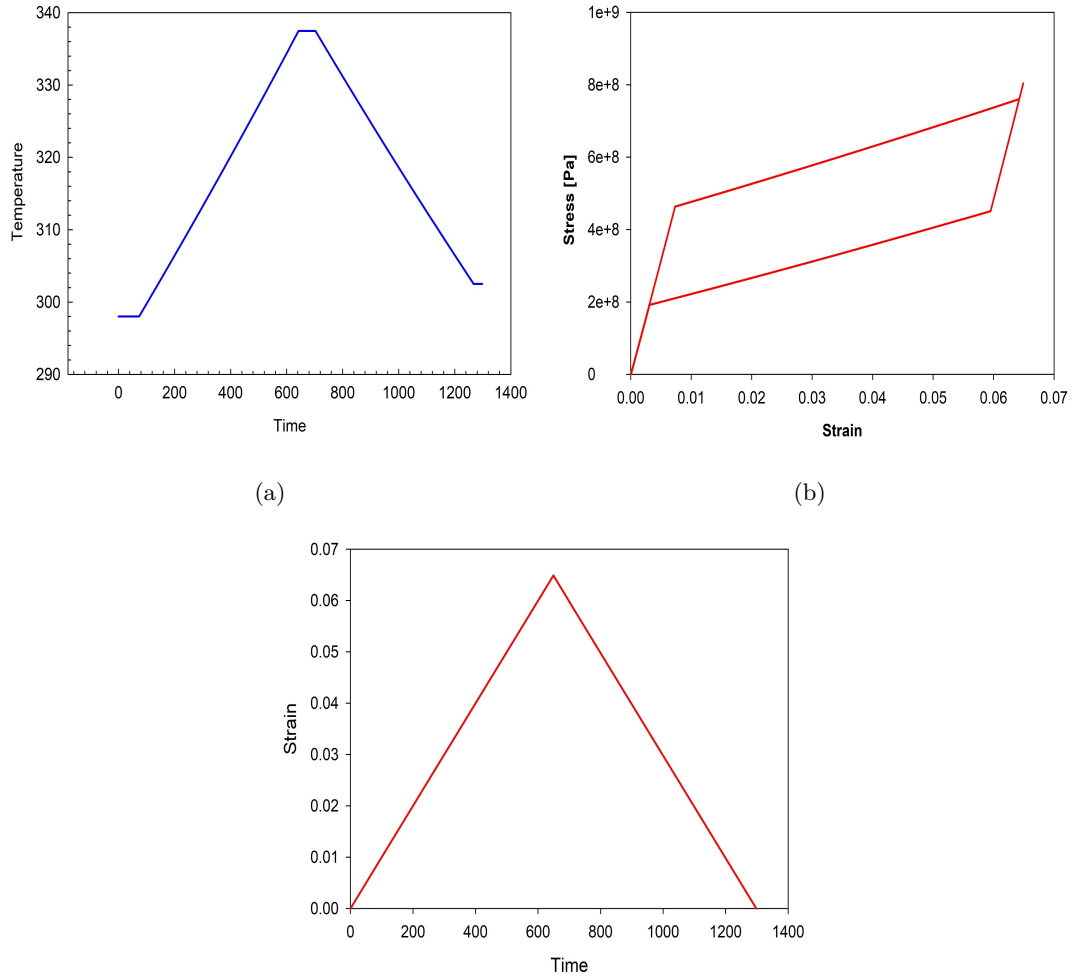

(a) (b)

(c)

Figure 4.9: Fully-coupled behavior of the model under uniaxial loading-unloading tensile stress. (a) Temperature-time plot, (b) stress-strain plot, and (c) strain-time plot, at the end of cycle

in Figure 4.10(a). As mentioned previously, constant a and J_3, are responsible for the ATC trend in our model. Figure 4.10(a) indicates the following facts:

- Stress value required to initiate the forward-reverse phase transformation is higher in compression.
- Hysteresis loop is wider in compression.
- Transformation strain measured in compression is less than the transformation strain measured in tension.

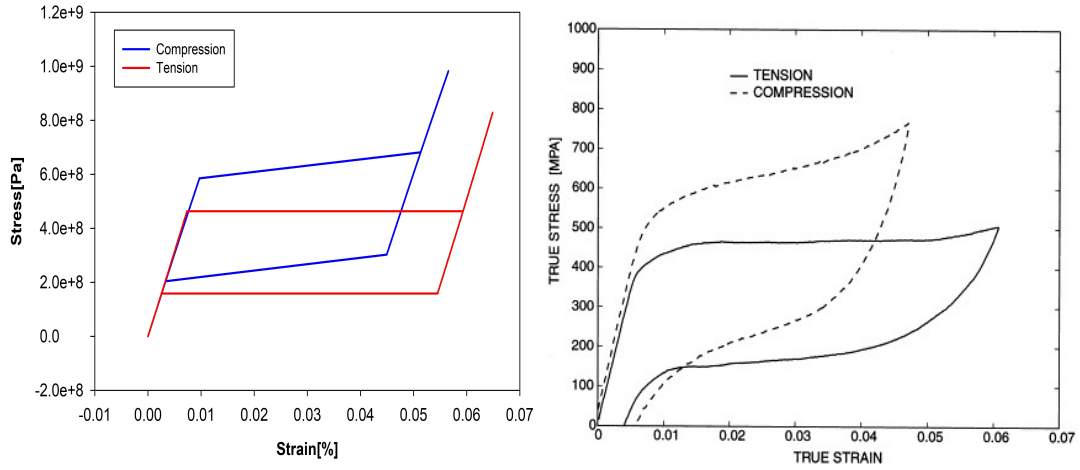

(a) (b)

Figure 4.10: (a) Numerical simulation of asymmetry in tension and compression, (b) Experimental results of ATC in pseudoelasticity obtained from Thamburaja and Anand [69].

As it is obvious from the plots 4.10(a) and 4.10(b), the results of our constitutive model and experimental findings are in well agreement with each other. The story behind the ATC is buried under the fact that under compressive stress large amount of dislocation happens between martensite bands; However, under tensile stress reorienting of martensite variants happens rather that generating dislocation.

4.4 One-way shape memory effect

The most prominent behavior of SMA, which makes it ideal for various applications, is one-way shape memory effect. When subjected to mechanical loading, a crystal structure of an initially twinned martensite becomes detwinned martensite and then by subsequent heating, it transforms to austenite structure. Here, a fully-coupled analysis conducted on the finite element model as following: initially, a concentrated force of 150 N applied to every single node in the z direction while temperature is below martensite finish temperature ($\theta = 240 < M_f$). Loading step continues until the whole material becomes fully austenitic. Then, material unloads to zero stress while ambient temperature is still ($\theta = 240 < M_f$). This is followed by heating to ($\theta = 298 > \theta_{af}$) and

subsequent cooling to ($\theta = 240 < M_f$), while the stress state is kept at zero. Figure 4.11, demonstrates a fine comparison among different numerical models and experimental findings of one-way effect in Ni-Ti SMA.

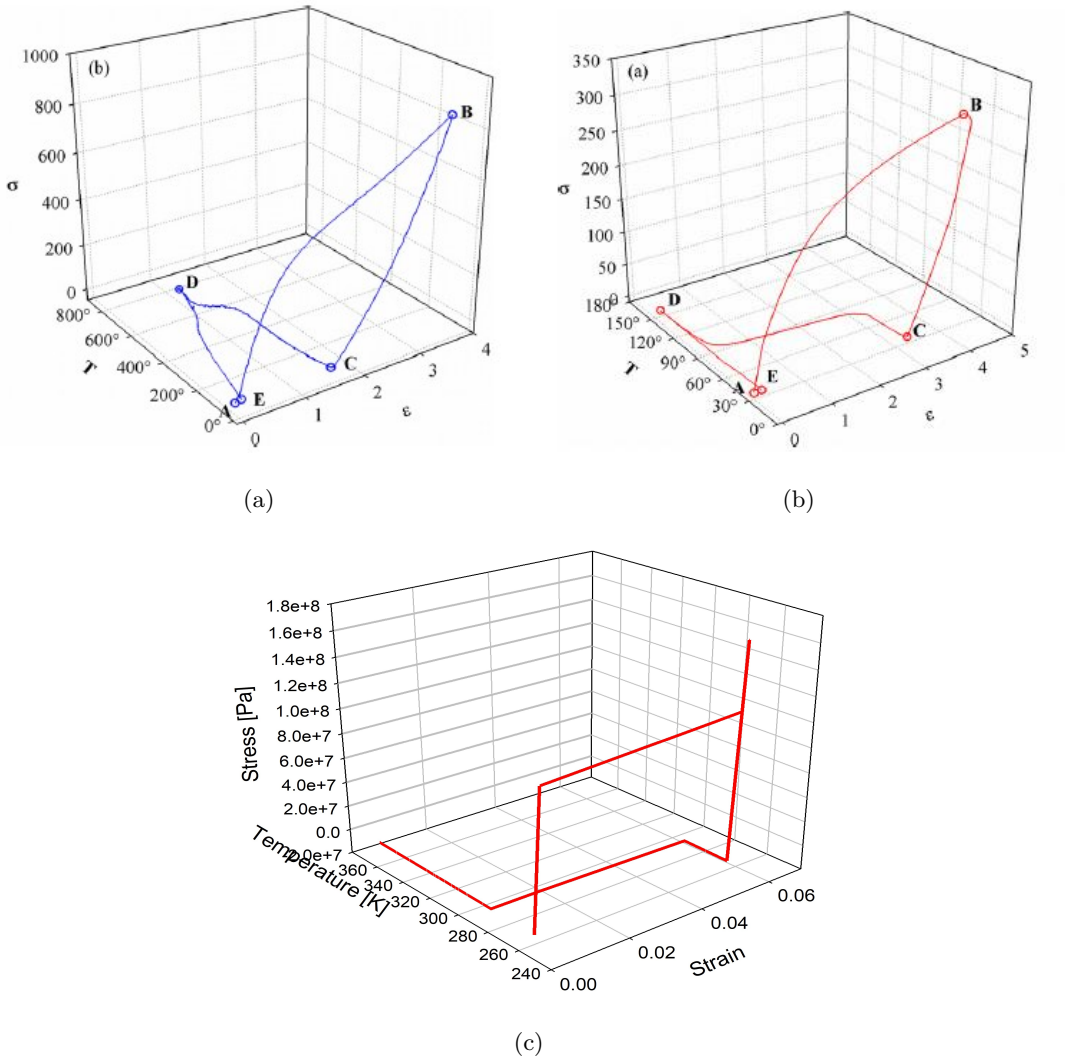

(a) (b)

(c)

Figure 4.11: (a)Experimental results obtained by Noebe et al [74] (b) model prediction of Saleeb et al. [9], (c) simulation results of numerical analysis.

Taking the importance of application of SMA helical actuators in electrical and aerospace industries into consideration, we implemented our constitutive model on the helical spring finite element mesh, as illustrated in Figure 4.2. Geometry is sketched by SolidWorks (2016), based on the parameters listed in Table 4.2, and then inserted to Abaqus/Implicit (2016) in order to be meshed. For detailed information about mesh configuration, reader is referred to section 4.1. Figure 4.12(a), indicates the helical spring at the beginning of analysis. Subjected to

uniaxial loading, spring elongates (see 4.12(b)), and subsequent unloading leads to driving back the elastic deformation as presented in the configuration 4.12(c). Next, pure thermal step begins as temperature raises from $240\,K$ to $340\,K$. By increasing temperature, spring shrinks to its initial shape as the residual plastic strain disappear, Figure 4.12(e). Here, stress, strain, and temperature-variation contours along the helical spring is clearly observable. Results of numerical simulations successfully signifies the prominent one-way shape memory effect.

4.5 Stress-controlled thermal cycling

Another manifestation of the pseudoelasticity response is the strain-temperature response under isobaric (constant stress) tension. A single element cube is subjected to fixed stress level of 80 MPa and goes through a single cycle of temperature between $265\,K$ and $320\,K$. The material initially is in full austenitic state; however, subsequent stress results in fully martensitic phase. This is followed by a raise in temperature to $320\,K$ and ended by decreaseing temperature to initial temperature $265K$. Padula et al. [75, 76], conducted different experiments on the thermal cycling of Ni-Ti SMA to demonstrate the evolutionary effect of this alloy. Figure 4.13, exhibits strain-temperature curve for isobaric tension obtained by experimental findings of Padula et al. [75, 76], model predictions of Anand and Gurtin [53], and our simulation results.

We also carried out a different simulation with different stress levels of 60 MPa to 130 MPa It is been concluded that increasing stress level leads to an increase in the initial temperature needed to initiate martensitic forward and reverse transformation. It is clear that thermal loop width remains fixed as stress increases i.e., it is independent of stress level at which transforamtion begins. Figure 4.14, compare the results of numerical simulation with experimental findings of Thamburaja and Anand [77].

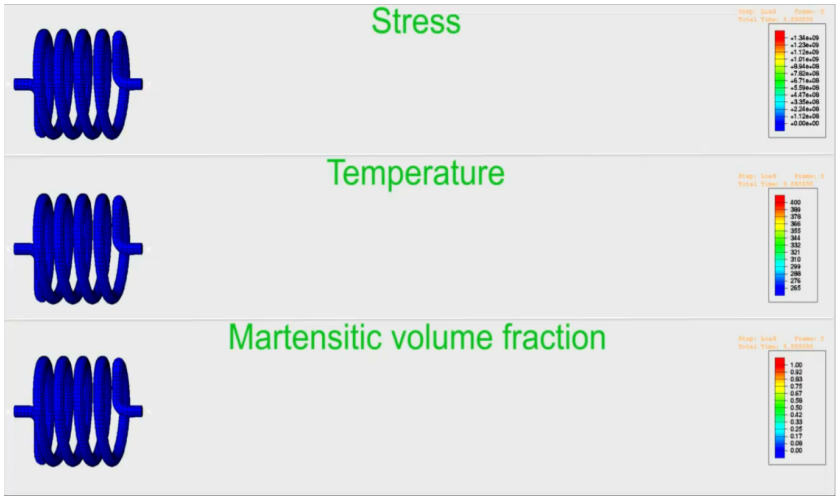

(a)

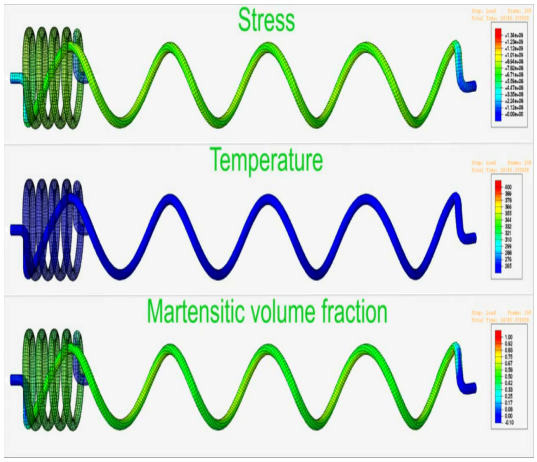

(b)

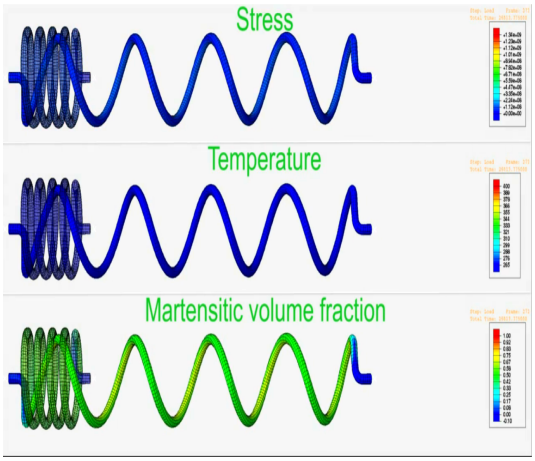

(c)

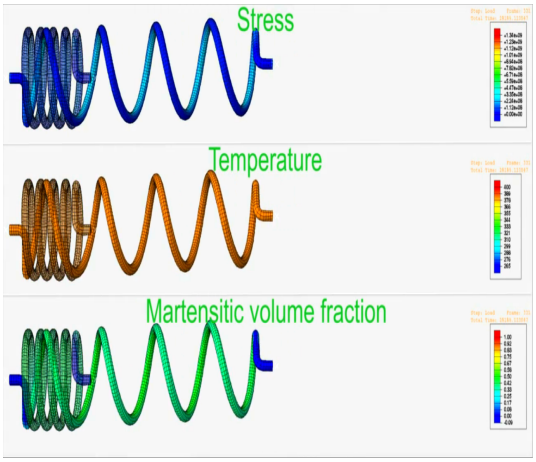

(d)

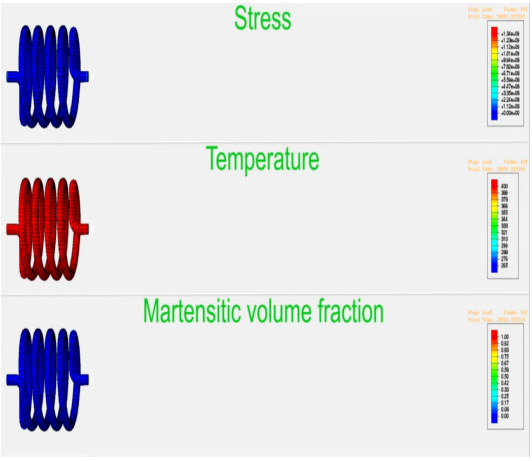

(e)

.

Figure 4.12: Finite element model of helical spring, implemented with constitutive model of polycrytalline Ni-Ti SMA. (a) Initial configuration, (b) end of loading step, (c) end of unloading step, (d) increasing temperature from $240K$ to $320K$, (e) end of heating step.

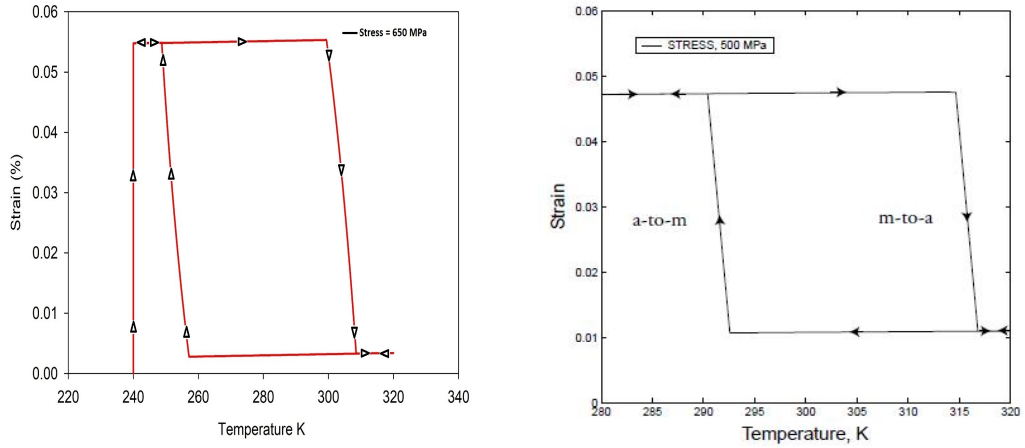

(a) (b)

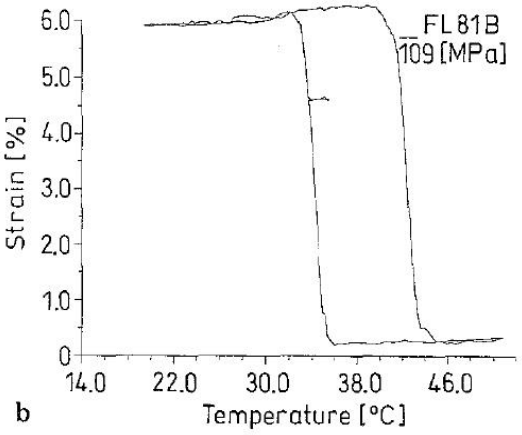

(c)

Figure 4.13: Single thermal cycle under isobaric stress. (a) Simulation results of our constitutive model, (b) model prediction of Thamburaja and Anand [53], (c) experimental results obtained by Saleeb et al. [71]

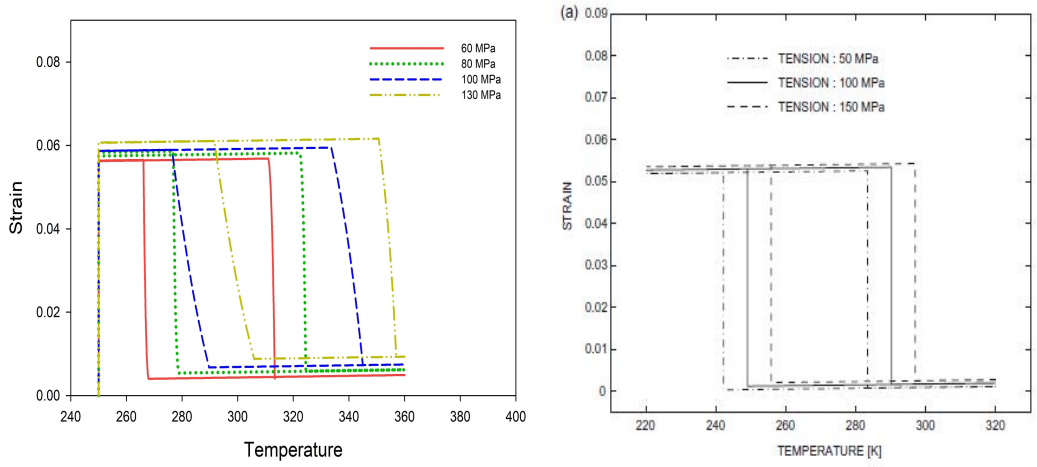

(a) (b)

Figure 4.14: Comparison of single thermal cycle under isobaric stress of various stresses. (a) result of numerical simulations, (b) model predictions of Thamburaja [65]

CHAPTER 5

CONCLUSION

To establish a constitutive theory for Ni-Ti SMA, this work utilized finite strain plasticity setting with purely thermodynamically consistent constitutive equations. With the martenesitic volume fraction as the internal variable evolving with phase transformation, our model demonstrated high capabilities in capturing various qualitative behavior of Ni-Ti SMA. The results show that SMAs can be modeled successfully within this framework. Delicate inspection in the temperature evolution equation and synchronizing it properly with the algorithm led us to reproduce the thermo-mechanically coupled behavior in a fundamental way.

It is shown that the presented constitutive model can perfectly capture pseudoelasticity, and one-way shape memory effect from different aspects. Furthermore, basics of the ATC is also reproduced by the derived constitutive model and it is in good agreement with experimental findings. Rate and temperature dependency is also captured successfully in presented constitutive model. In this thesis, both isothermal and coupled simulations conducted on different 2-D and 3-D finite element mesh and implemented to ABAQUS/Implicit (2016) finite element program. Although, SMAs are mostly subjected to large scale deformations, most constitutive models existed in the literature are written in small strain framework which can not intricately reproduce the related phenomena. Some of these classically well-known models do not function in a fully-coupled manner. They mostly introduce an internal variable to be responsible for the temperature evolution of model. In this regard, we put our effort to establish

constitutive relations which are able to successfully model important behaviors of SMAs such as martensitic phase transformation, pseudoelasticity, and one-way shape memory effect under different loading and temperature conditions.

In the light of obtained results, next step will be to further investigate the model under different proportional-unproportional multiaxial loading conditions.

REFERENCES

[1] Young Ik Yoo Lim, Jung Ju Lee, Chang Ho Lee, and Jae Hyuk. An experimental study of the two-way shape memory effect in a NiTi tubular actuator. *Smart Materials and Structures*, 19(12):125002, 2010.

[2] Andrzej Ziolkowski. *Pseudoelasticity of Shape Memory Alloys: Theory and Experimental Studies*. Butterworth-Heinemann,, 2015.

[3] D.C. Lagoudas. *Shape Memory Alloys-Modeling and Engineering Applications*. Springer US, 2008.

[4] Z Bo and D C Lagoudas. Thermomechanical modeling of polycristaline SMAs under cyclic loading, Part I: theroretical derivations. *International Journal of Engineering Science*, 37(March 1997):1089–1140, 1999.

[5] Kaushik Bhattacharya. *Microstructure of Martensite: Why It Forms and How It Gives Rise to the Shape-Memory Effect*. Oxford University Press, 2004.

[6] Yildirim Aydogdu, Ayse Aydogdu, and Osman Adiguzel. Self-accommodating martensite plate variants in shape memory CuAlNi alloys. *Journal of Materials Processing Technology*, 123(3):498–500, 2002.

[7] C. M. Wayman K. Otsuka. *Shape memory materials*. Cambridge University Press, 1999.

[8] C. M. Wayman. T. W. Duerig, K. N. Melton, D. Stöckel. *Engineering Aspects of Shape Memory Alloys*, volume 1. Butterworth-Heinemann,, 1990.

[9] A. F. Saleeb, S. A. Padula, and A. Kumar. A multi-axial, multimechanism based constitutive model for the comprehensive representation of the evolutionary response of SMAs under general thermomechanical loading conditions. *International Journal of Plasticity*, 27(5):655–687, 2011.

[10] S. Gollerthan, D. Herberg, A. Baruj, and G. Eggeler. Compact tension testing of martensitic/pseudoplastic NiTi shape memory alloys. *Materials Science and Engineering A*, 481-482(1-2 C):156–159, 2008.

[11] J. Ma, I. Karaman, and R. D. Noebe. High temperature shape memory alloys. *International Materials Reviews*, 55(5):257–315, 2010.

[12] A. Yawny E. Cingolani and M. Ahlers. The Two Way Shape Memory Effect in Stabilized and Pseudoelastically Trained Cu-Zn-Al Single Crystals. *Journal de Physique IV*, 05:865–869, 1995.

[13] Horst Biermann Thomas Niendorf, Florian Brenne, Philipp Krooß, Malte Vollmer, Johannes Günther, Dieter Schwarze. Microstructural Evolution and Functional Properties of Fe-Mn-Al-Ni Shape Memory Alloy Processed by Selective Laser Melting. *Metallurgical and Materials Transactions A*, 47(6):2569—-2573, 2016.

[14] M S Alam, M A Youssef, and M Nehdi. Utilizing shape memory alloys to enhance the performance and safety of civil infrastructure : a review. *Canadian Journal of Civil Engineering*, 34(9):1075–1086, 2007.

[15] Raghavendra R. Adharapurapu, Fengchun Jiang, Kenneth S. Vecchio, and George T. Gray. Response of NiTi shape memory alloy at high strain rate: A systematic investigation of temperature effects on tension-compression asymmetry. *Acta Materialia*, 54(17):4609–4620, 2006.

[16] G. S. Firstov, Yu N. Koval, J. Van Humbeeck, and P. Ochin. Martensitic transformation and shape memory effect in Ni3Ta: A novel high-temperature shape memory alloy. *Materials Science and Engineering A*, 481-482(1-2 C):590–593, 2008.

[17] K Gall. On the mechanical behavior of single crystal NiTi shape memory alloys and related polycrystalline phenomenon. *Materials Science and Engineering A*, 317(1-2):85–92, 2001.

[18] G Xu. Structural defects of Pb(Mg1/3Nb2/3)O3–PbTiO3 single crystals grown by a Bridgman method. *Journal of Crystal Growth*, 222(1-2):202–208, 2001.

[19] Guisheng Xu, Haosu Luo, Yiping Guo, Yuqi Gao, Haiqing Xu, Zhenyi Qi, Weizhuo Zhong, and Zhiwen Yin. Growth and piezoelectric properties of Pb(Mg1/3Nb2/3)O3-PbTiO3 crystals by the modified Bridgman technique. *Solid State Communications*, 120(7-8):321–324, 2001.

[20] C. Lexcellent and H. Tobushi. Internal loops in pseudoelastic behaviour of Ti-Ni shape memory alloys: Experiment and modelling. *Meccanica*, 30(5):459–466, 1995.

[21] K. K. Kitamura Tanaka. Shape memory alloy preparation for multiaxial tests and identification of fundamental alloy performance. *Archives of Mechanics*, 51(6):785–803, 1999.

[22] Yong Liu, Z Xie, J Van Humbeeck, and L Delaey. Asymmetry of stress–strain curves under tension and compression for NiTi shape memory alloys. *Acta Materialia*, 46(12):4325–4338, 1998.

[23] J. Rejzner, C. Lexcellent, and B. Raniecki. Pseudoelastic behaviour of shape memory alloy beams under pure bending: Experiments and modelling. *International Journal of Mechanical Sciences*, 44(4):665–686, 2002.

[24] John A. Shaw and Stelios Kyriakides. Thermomechanical aspects of NiTi. *Journal of the Mechanics and Physics of Solids*, 43(8):1243–1281, 1995.

[25] Cliff J. Lissenden, Devaraj Doraiswamy, and Steven M. Arnold. Experimental investigation of cyclic and time-dependent deformation of titanium alloy at elevated temperature. *International Journal of Plasticity*, 23(1):1–24, 2007.

[26] B. Kockar, I. Karaman, J. I. Kim, Y. I. Chumlyakov, J. Sharp, and C. J (Mike) Yu. Thermomechanical cyclic response of an ultrafine-grained NiTi shape memory alloy. *Acta Materialia*, 56(14):3630–3646, 2008.

[27] C. Grabe and O. T. Bruhns. On the viscous and strain rate dependent behavior of polycrystalline NiTi. *International Journal of Solids and Structures*, 45(7-8):1876–1895, 2008.

[28] C. Grabe and O. T. Bruhns. Path dependence and multiaxial behavior of a polycrystalline NiTi alloy within the pseudoelastic and pseudoplastic temperature regimes. *International Journal of Plasticity*, 25(3):513–545, 2009.

[29] Gerhard A. Holzapfel, D.C. Lagoudas, and William S. Slaughter. *The Linearized Theory of Elasticity*. Wiley, 2012.

[30] Gerhard A. Holzapfel. *Nonlinear Solid Mechanics: A Continuum Approach for Engineering*. Wiley, 2000.

[31] F Falk. Model free energy, mechanics, and thermodynamics of shape memory alloys. *Acta Metallurgica*, 28(12):1773–1780, 1980.

[32] F. Falk. Ginzburg-Landau theory of static domain walls in shape-memory alloys. *Zeitschrift fur Physik B Condensed Matter*, 51(2):177–185, 1983.

[33] J. M. Ball and R. D. James. Fine phase mixtures as minimizers of energy. *Archive for Rational Mechanics and Analysis*, 100(1):13–52, 1987.

[34] G. R. Barsch and J. a. Krumhansl. Nonlinear and nonlocal continuum model of transformation precursors in martensites. *Metallurgical Transactions A*, 19(4):761–775, 1988.

[35] Rohan Abeyaratne and James K. Knowles. A continuum model of a thermoelastic solid capable of undergoing phase transitions. *Journal of the Mechanics and Physics of Solids*, 41(3):541–571., 1993.

[36] W S Lai and B X Liu. Lattice stability of some Ni-Ti alloy phases versus their chemical composition and disordering. *Journal of Physics: Condensed Matter*, 12(5):L53, 2000.

[37] Graeme J. Ackland, A. P. Jones, and R. Noble-Eddy. Molecular dynamics simulations of the martensitic phase transition process. *Materials Science and Engineering A*, 481-482(1-2 C):11–17, 2008.

[38] Takuya Uehara & Takato Tamai. An Atomistic Study on Shape-Memory Effect by Shear Deformation and Phase Transformation. *Mechanics of Advanced Materials and Structures*, 13(2):197–204, 2006.

[39] Oliver Kastner, Gunther Eggeler, Wolf Weiss, and Graeme J. Ackland. Molecular dynamics simulation study of microstructure evolution during cyclic martensitic transformations. *Journal of the Mechanics and Physics of Solids*, 59(9):1888–1908, 2011.

[40] Kikuaki Tanaka, F. Nishimura, M. Matsui, H. Tobushi, and Pin Hua Lin. Phenomenological analysis of plateaus on stress-strain hysteresis in TiNi shape memory alloy wires. *Mechanics of Materials*, 24(1):19–30, 1996.

[41] Michael I Barbarino, Silvestro and Flores, EI Saavedra and Ajaj, Rafic M and Dayyani, Iman and Friswell. A review on shape memory alloys with applications to morphing aircraft. *Smart Materials and Structures*, 23(6):063001, 2014.

[42] M. Bodaghi, A. R. Damanpack, M. M. Aghdam, and M. Shakeri. A phenomenological SMA model for combined axial-torsional proportional/non-proportional loading conditions. *Materials Science and Engineering: A*, 587:12–26, 2013.

[43] Etienne Patoor, Dimitris C. Lagoudas, Pavlin B. Entchev, L. Catherine Brinson, and Xiujie Gao. Shape memory alloys, Part I: General properties and modeling of single crystals. *Mechanics of Materials*, 38(5-6):391–429, 2006.

[44] Kiyohide Wada and Yong Liu. On the two-way shape memory behavior in NiTi alloy-An experimental analysis. *Acta Materialia*, 56(13):3266–3277, 2008.

[45] K. Wada and Yong Liu. Thermomechanical training and the shape recovery characteristics of NiTi alloys. *Materials Science and Engineering A*, 481-482(1-2 C):166–169, 2008.

[46] Darren J. Hartl, George Chatzigeorgiou, and Dimitris C. Lagoudas. Three-dimensional modeling and numerical analysis of rate-dependent irrecoverable deformation in shape memory alloys. *International Journal of Plasticity*, 26(10):1485–1507, 2010.

[47] Yves Chemisky, George Chatzigeorgiou, Parikshith Kumar, and Dimitris C. Lagoudas. A constitutive model for cyclic actuation of high-temperature shape memory alloys. *Mechanics of Materials*, 68:120–136, 2014.

[48] Halphen, Bernard and Nguyen quoc Son. Plastic and visco-plastic materials with generalized potential. *Mechanics Research Communications*, 1(1):43–47, 1974.

[49] Wael Zaki and Ziad Moumni. A three-dimensional model of the thermomechanical behavior of shape memory alloys. *Journal of the Mechanics and Physics of Solids*, 55(11):2455–2490, 2007.

[50] Wael Zaki and Ziad Moumni. A 3D model of the cyclic thermomechanical behavior of shape memory alloys. *Journal of the Mechanics and Physics of Solids*, 55(11):2427–2454, 2007.

[51] Wael Zaki, Ziad Moumni, and Claire Morin. Modeling Tensile-compressive Asymmetry for Superelastic Shape Memory Alloys. *Mechanics of Advanced Materials and Structures*, 18(7):559–564, 2011.

[52] Ziad Moumni Wael Zaki, Xiojun Gu, Claire Morin. Time integration and assessment of a model for shape memory alloys considering multiaxial non-proportional loading cases. *International Journal of Solids and Structures*, 54:82–89, 2015.

[53] Lallit Anand and Morton E. Gurtin. Thermal effects in the superelasticity of crystalline shape-memory materials. *Journal of the Mechanics and Physics of Solids*, 51(6):1015–1058, 2003.

[54] P. Thamburaja and L. Anand. Superelastic behavior in tension-torsion of an initially-textured Ti-Ni shape-memory alloy. *International Journal of Plasticity*, 18(11):1607–1617, 2002.

[55] David L. Henann and Lallit Anand. A large deformation theory for rate-dependent elastic-plastic materials with combined isotropic and kinematic hardening. *International Journal of Plasticity*, 25(10):1833–1878, 2009.

[56] Ferdinando Auricchio and Robert L. Taylor. Shape-memory alloys: modelling and numerical simulations of the finite-strain superelastic behavior. *Computer Methods in Applied Mechanics and Engineering*, 143(1-2):175–194, 1997.

[57] G. Barot, I. J. Rao, and K. R. Rajagopal. A thermodynamic framework for the modeling of crystallizable shape memory polymers. *International Journal of Engineering Science*, 46(4):325–351, 2008.

[58] E. H. Lee. Elastic-plastic deformation at finite strains. In *Journal of Applied Mechanics*, volume 36. ASME, 1969.

[59] Morton E.Gurtin, Eliot Fried, and Lallit Anand. *The mechanics and thermodynamics of continua*. Cambridge University Press, 2010.

[60] Ekkehart Kröner. Allgemeine Kontinuumstheorie der Versetzungen und Eigenspannungen. *Archive for Rational Mechanics and Analysis*, 4(1):273–334, 1959.

[61] Morton E. Gurtin and Lallit Anand. The decomposition F = FeFp, material symmetry, and plastic irrotationality for solids that are isotropic-viscoplastic or amorphous. *International Journal of Plasticity*, 21(9):1686–1719, 2005.

[62] Qing Ping Sun. Author links open the author workspace.Keh Chih Hwang. Micromechanics modelling for the constitutive behavior of polycrystalline shape memory alloys—I. Derivation of general relations. *Journal of the Mechanics and Physics of Solids*, 41(1):1–17, 1993.

[63] L. Orgéas and D. Favier. Stress-induced martensitic transformation of a NiTi alloy in isothermal shear, tension and compression. *Acta Materialia*, 46(15):5579–5591, 1998.

[64] James G Boyd and Dimitris C Lagoudas. A thermodynamical constitutive model for shape memory materials. Part I. The monolithic shape memory alloy. *International Journal of Plasticity*, 12(6):805–842, 1996.

[65] P. Thamburaja. A finite-deformation-based phenomenological theory for shape-memory alloys. *International Journal of Plasticity*, 26(8):1195–1219, 2010.

[66] E. Gurtin E. Fried. Dynamic solid-solid transitions with phase characterized by an order parameter. *Physica D*, 72(4):287–308, 1994.

[67] Dirk Helm and Peter Haupt. Shape memory behaviour: Modelling within continuum thermomechanics. *International Journal of Solids and Structures*, 40(4):827–849, 2003.

[68] L. Orgéas and D. Favier. Stress-induced martensitic transformation of a NiTi alloy in isothermal shear, tension and compression. *Acta Materialia*, 46(15):5579–5591, 1998.

[69] P. Thamburaja and L. Anand. Polycrystalline shape-memory materials: Effect of crystallographic texture. *Journal of the Mechanics and Physics of Solids*, 49(4):709–737, 2001.

[70] Michael Smith. *ABAQUS/Standard User's Manual, Version 6.14*. SIMULIA, 2014.

[71] A. F Saleeb, B Dhakal, M S Hosseini, and S a Padula II. Large scale simulation of NiTi helical spring actuators under repeated thermomechanical cycles. *Smart Materials and Structures*, 22(9):094006, 2013.

[72] I. Müller Y. Huo. C0ntinuum NIechanics Nonequilibrium Thermodynamics of Pseudoelasticity. *Continuum mechanics and Thermodynaics*, 5:163–204, 1993.

[73] T. Jesse Lim McDowell and David L. Mechanical Behavior of an Ni-Ti Shape Memory Alloy Under Axial-Torsional Proportional and Nonproportional Loading. *Engineering Materials and Technology*, 121(1):9–18, 1999.

[74] Ronald Noebe ; Darrell Gaydosh ; Santo Padula II ; Anita Garg ; Tiffany Biles ; Michael Nathal. Properties and potential of two (Ni,Pt)Ti alloys for use as high-temperature actuator materials. *Smart Structures and Materials 2005: Active Materials: Behavior and Mechanics, 364 (May 20, 2005);*, 2005.

[75] Padula, Shipeng Qiu, Darrell J Gaydosh, Ronald D Noebe, Glen S Bigelow, Anita Garg, R A J Vaidyanathan, Santo A Padula, Darrell J Gaydosh, Ronald D Noebe, Glen S Bigelow, Anita Garg, Dimitris Lagoudas, Ibrahim Karaman, Kadri C Atli, and Brookpark Rd. Influence of Test Procedures on the Thermomechanical Properties of a 55NiTi Shape Memory Alloy. In *The 15th International Symposium on: Smart Structures and Materials & Nondestructive Evaluation and Health Monitoring.*, volume 6929, pages 1–11. International Society for Optics and Photonics, 2008.

[76] Padula, Shipeng Qiu, Darrell Gaydosh, Ronald Noebe, Glen Bigelow, Anita Garg, and R A J Vaidyanathan. Effect of Upper-Cycle Temperature on the Load-Biased , Strain-Temperature Response of NiTi. *Metallurgical and Materials Transactions A*, 43(12):4610–4621, 2012.

[77] P. Thamburaja and L. Anand. Thermo-mechanically coupled superelastic response of initially-textured Ti-Ni sheet. *Acta Materialia*, 51(2):325–338, 2003.

APPENDIX A

TIME-INTEGRATION PROCEDURE : CONSTITUTIVE MODEL OF NI-TI SHAPE MEMORY ALLOY

This appendix, gives a comprehensive summary on the implicit time-integration procedure of constitutive model developed for Ni-Ti SMA. Here, t denotes the current time, Δt is an infinitesimal time increment, and $\tau = t + \Delta t$.

Following parameters are known at the beginning of each step in the algorithm:

- $\mathbf{F}(t)$, $\mathbf{F}(\tau)$, $\theta(t)$, $\theta(\tau)$.
- $\mathbf{T}(t)$, $\mathbf{F}^p(t)$.
- $\mathbf{B}(t)$, $\mathbf{N}_1(t)$, $\mathbf{N}_2(t)$, $\phi(t)$.
- Martensite volume fraction $\xi(t)$.

note that, initially $\mathbf{B}(t) = \mathbf{0}$.

Following parameters will be calculated at the end of the each step:

- $\mathbf{T}(\tau)$, $\mathbf{F}^p(\tau)$.
- $\mathbf{B}(\tau)$, $\mathbf{N}_1(\tau)$, $\mathbf{N}_2(\tau)$, $\phi(\tau)$.
- Martensitic volume fraction $\xi(\tau)$ with advancing forward in time.

The steps of algorithm are as follows:

Step 1. Calculate the trial elastic strain $\mathbf{E}^e(\tau)^{\text{trial}}$:

$$\begin{aligned}
\mathbf{F}^e(\tau)^{\text{trial}} &= \mathbf{F}(\tau)\mathbf{F}^p(t)^{-1}, \\
\mathbf{C}^e(\tau)^{\text{trial}} &= (\mathbf{F}^e(\tau)^{\text{trial}})^T\mathbf{F}^e(\tau)^{\text{trial}}, \\
\mathbf{E}^e(\tau)^{\text{trial}} &= (1/2)(\mathbf{C}^e(\tau)^{\text{trial}} - \mathbf{1}).
\end{aligned}$$

Step 2. Calculate the trial stress $\mathbf{T}^*(\tau)^{\text{trial}}$

$$\mathbf{T}^*(\tau)^{\text{trial}} = 2\mu\mathbf{E}_0^e(\tau)^{\text{trial}} + \kappa[\text{tr}\mathbf{E}^e(\tau)^{\text{trial}} - 3\alpha_{\text{th}}(\theta(\tau) - \theta_0)]\mathbf{1} \tag{A.1}$$

Step 3. Calculate the trial driving forces $f_i(\tau)^{\text{trial}}$. In our implicit numerical algorithm , initially we approximate:

$$\mathbf{N}_i(\tau) \approx \mathbf{N}_i(t), \quad \phi(\tau) \approx \phi(t) \quad \text{and} \quad \bar{\mathbf{T}}(\tau) \approx \mathbf{T}^*(\tau) \tag{A.2}$$

Note that later approximation is valid only in infinitesimal elastic stretches. Thus, the trial driving force for phase transformation are then given by:

$$f_i(\tau) = \sqrt{\frac{3}{2}}(1 + a\phi(t)) \left[\mathbf{T}_0^*(\tau)^{\text{trial}} \cdot \mathbf{N}_i(t)\right] - \frac{\lambda_T}{\theta_T}(\theta(\tau) - \theta_T) - h\xi(t) \tag{A.3}$$

Step 4. Evolution equation for plastic decomposition of deformation matrix.
lets take plastic distortion-rate tensor, Eq. (3.41):

$$\mathbf{L}^p = \sqrt{3/2}(1 + a\phi)\sum_{i=1}^{2}\dot{\xi}_i\mathbf{N}_i$$

and putting it into the decomposition of distortion-rate tensor, $\mathbf{L}^p = \dot{\mathbf{F}}^p\mathbf{F}^{p-1}$ yields,

$$\mathbf{F}^p(\tau) = \left\{\mathbf{1} + \sqrt{3/2}(1 + a\phi(t))\sum_{i=1}^{2}\Delta\xi_j\mathbf{N}_j(t)\right\}\mathbf{F}^p(t) \tag{A.4}$$

Step 5. Determine the criteria for potential transformation systems.
Consistency conditions for phase transformation are as follows:

- For forward transformation,

$$f_1(\tau) - f_c = 0$$

- For reverse transformation,

$$f_2(\tau) + f_c = 0$$

Using Eqs. (A.1)-(A.4), it is straightforward to show that:

$$f_i(\tau) = f_i(\tau)^{\text{trial}} - \sum_{i,j=1}^{2} \Delta\xi_j \left[3\mu(1+a\phi(t))^2 \text{sym}(\mathbf{C}^e(\tau)^{\text{trial}}\mathbf{N}_j(t)) \cdot \mathbf{N}_i(t) + h\delta_{ij}\right] \tag{A.5}$$

where δ_{ij} is the Kronecker delta. Substituting Eq. (A.5) into mentioned above consistency equations yields transformation conditions as follows:

$$\left[3\mu(1+a\phi(t))^2\mathbf{N}_i(t) \cdot \text{sym}(\mathbf{C}^e(\tau)^{\text{trial}}\mathbf{N}_j(t)) + h\delta_{ij}\right] \Delta\xi_i = b_i \quad \text{with } i,j = 1,2 \tag{A.6}$$

for forward transformation,

$$b_1 = f_1(\tau)^{\text{trial}} - f_c > 0 \quad \text{and} \quad \Delta\xi_1 > 0$$

for reverse transformation,

$$b_2 = f_2(\tau)^{\text{trial}} + f_c < 0 \quad \text{and} \quad \Delta\xi_1 < 0$$

For the considerations of rate dependency, we define a subroutine that iteratively solve for the martensitic volume change rate using Newton-Raphson/Bisection method. For the detailed information, reader is referred to numerical recipe of RTSAFE function. By taking Eqs. 2.57 and 2.58 into consideration, function $f(x)$ to be used in the algorithm is:

$$f(x) = f_1(\tau)^{\text{trial}} - \left[3\mu(1+a\phi(t))^2\mathbf{N}_1(t) \cdot \text{sym}(\mathbf{C}^e(\tau)^{\text{trial}}\mathbf{N}_1(t)) + h\right] \Delta\xi_1(\tau) - f(c)\left(\frac{\Delta\xi_1(\tau)}{\Delta\xi_1(t)}\right)^m \tag{A.7}$$

for forward transformation, and:

$$f(x) = f_2(\tau)^{\text{trial}} - \left[3\mu(1+a\phi(t))^2\mathbf{N}_2(t) \cdot \text{sym}(\mathbf{C}^e(\tau)^{\text{trial}}\mathbf{N}_2(t)) + h\right] \Delta\xi_2(\tau) - f(c)\left(\frac{\Delta\xi_2(\tau)}{\Delta\xi_2(t)}\right)^m \tag{A.8}$$

for reverse transformation. Here m is the parameter for controlling the amount of rate-dependency.

Step 6. Update the martensitic volume fraction.

$$\xi(\tau) = \xi(t) + \sum_i \Delta\xi_i, \quad i = 1,2 \tag{A.9}$$

If $\xi(\tau) > 1$, then set $\xi(\tau) = 1$. If $\xi(\tau) < 0$, then set $\xi(\tau) = 0$.

Step 7. Update the plastic distortion $\mathbf{F}^p(\tau)$.

$$\mathbf{F}^p(\tau) = \left\{ \mathbf{1} + \sqrt{3/2}(1 + a\phi(t) \sum_{i=1}^{2} \Delta\xi_j \mathbf{N}_j(t) \right\} \mathbf{F}^p(t) \tag{A.10}$$

Step 8. Calculate the stress $\mathbf{T}^*(\tau)$.

$$\begin{aligned} \mathbf{F}^e(\tau) &= \mathbf{F}(\tau)\mathbf{F}^p(\tau)^{-1}, \\ \mathbf{C}^e(\tau) &= (\mathbf{F}^e(\tau))^T \mathbf{F}^e(\tau), \\ \mathbf{E}^e(\tau) &= (1/2)(\mathbf{C}^e(\tau) - \mathbf{1}), \\ \mathbf{T}^*(\tau) &= 2\mu \mathbf{E}_0^e(\tau) + \kappa[\mathrm{tr}\mathbf{E}^e(\tau) - 3\alpha_{\mathrm{th}}(\theta(\tau) - \theta_0)]\mathbf{1} \end{aligned} \tag{A.11}$$

Step 9. Update the flow direction $\mathbf{N}_1(\tau)$ and the J-3 parameter.

$$\mathbf{N}_1(\tau) = \epsilon_T \left[\frac{\mathbf{T}_0^*(\tau)}{|\mathbf{T}_0^*(\tau)|} \right] \quad \text{and} \quad \phi(\tau) = \sqrt{6} \left[\mathbf{N}_1(\tau) \cdot (\mathbf{N}_1(\tau))^2 \right] (\epsilon_T)^{-3} \tag{A.12}$$

Step 10. Update the tensors $\mathbf{B}(\tau)$ and reverse flow direction $\mathbf{N}_2(\tau)$:

$$\mathbf{B}(\tau) = \mathbf{B}(t) + \sqrt{3/2}(1 + a\phi(t) \sum_{i=1}^{2} \Delta\xi_j \mathbf{N}_j(t) \quad \text{and} \quad \mathbf{N}_2(\tau) = \epsilon_T \left[\frac{\mathbf{B}(\tau)}{|\mathbf{B}(\tau)|} \right] \tag{A.13}$$

Step 11. Calculate the driving forces $\mathbf{f}_i(\tau)$

$$f_i(\tau) = \sqrt{\frac{3}{2}}(1 + a\phi(t)) \left[\mathbf{T}_0^*(\tau) \cdot \mathbf{N}_i(\tau) \right] - \frac{\lambda_T}{\theta_T}(\theta(\tau) - \theta_T) - h\xi(\tau) \tag{A.14}$$

Step 12. Calculate the inelastic work increment:

$$\Delta\omega^p = \left(\frac{\lambda_T}{\theta_T} \right) \theta(\tau) \sum_i \Delta\xi_i - 3\kappa\alpha_{\mathrm{th}}\theta(\tau)(\mathrm{tr}(\Delta\mathbf{E}^e)) + \sum_i f_i(\tau)\Delta\xi_i \tag{A.15}$$

Inelastic work increment causes heating/cooling during deformation.

Step 13. Calculate the Cauchy stress $\mathbf{T}(\tau)$:

$$\mathbf{T}(\tau) = [\det\mathbf{F}(\tau)]^{-1} \mathbf{F}^e(\tau)\mathbf{T}^*(\tau)\mathbf{F}^e(\tau)^T \tag{A.16}$$

In this algorithm, elastic and numerical tangent matrices have been introduced in order to be utilized in the UMAT code.